energies

MDPI

Article

Surrogate-Assisted Multi-Objective Optimization of Engine-Level Pneumatic Assistance for Arctic Diesel Generators †

Joseph K. Basakayi [1], Eudes K. Tshitshonu [1,2], Daniel R. Rousse [1] and Adrian Ilinca [1,*]

[1] L3E Research Group, Mechanical Engineering Department, École de Technologie Supérieure, Montréal, QC H3C 1K3, Canada; joseph-kantole.basakayi.1@ens.etsmtl.ca (J.K.B.); eudes-tshitshonu.kabeya.1@ens.etsmtl.ca (E.K.T.); daniel.rousse@etsmtl.ca (D.R.R.)

[2] Mechanical Engineering Department, Vaal University of Technology, Andries Potgieter Blvd, Vanderbijlpark 1911, South Africa

* Correspondence: adrian.ilinca@etsmtl.ca

† This paper is an extended version of our paper published in 3rd International Online Conference on Energies (IOCEN 2026), 12–15 May 2026. An earlier version of this work was presented at the 3rd International Online Conference on Energies (IOCEN 2026), 12–15 May 2026. The present manuscript substantially extends the conference paper through a comprehensive literature review, expanded methodological development, Gaussian Process surrogate modeling, Sobol global sensitivity analysis, deterministic multi-objective optimization, SIMUS-based decision making, extensive validation, uncertainty analysis, and a significantly expanded discussion.

Abstract

Diesel generators remain indispensable for supplying reliable electricity in isolated Arctic microgrids, where harsh environmental conditions, high fuel transportation costs, and stringent emission requirements motivate improvements in engine performance and environmental sustainability. This study proposes and validates a unified, surrogate-assisted tri-objective optimization framework to calibrate the engine operation of a pneumatically assisted CAT 3516 diesel generator under representative Arctic conditions at Raglan Mine, Canada. The optimization focuses on engine-level pneumatic assistance, while compressed air generation, storage, and distribution are outside the scope of the study. The framework integrates high-fidelity Diesel-RK simulations, adaptive Sobol sampling, Gaussian Process surrogate modeling with predictive uncertainty, global sensitivity analysis, deterministic multi-objective optimization, SIMUS-based Pareto ranking, and independent high-fidelity validation. We optimized three engine-control variables (start of injection, compressor pressure ratio, and fuel mass per cycle) simultaneously to maximize brake power while minimizing brake-specific fuel consumption and NO_x emissions. The surrogate models achieved coefficients of determination exceeding 0.97 for brake power, brake-specific fuel consumption, and peak cylinder pressure, while the NO_x surrogate reached an R^2 of 0.82. The selected operating point reduced NO_x emissions by 26.9%, increased brake power by 3.7%, and increased brake-specific fuel consumption by only 0.87% relative to the Arctic baseline. The proposed uncertainty-aware framework provides a computationally efficient and reproducible methodology for engine-level calibration of pneumatically assisted diesel generators operating in isolated Arctic hybrid energy systems.

Keywords: Arctic microgrids; diesel generator; tri-objective surrogate optimization; Gaussian Process; Sobol sensitivity; NSGA-II; SIMUS; Diesel-RK; NO_x reduction; pneumatic hybridization

Check for updates

Academic Editors: Alessandro Niccolai and Constantine D. Rakopoulos

Received: 6 August 2026
Revised: 11 September 2026
Accepted: 7 October 2026
Published: 14 October 2026

Copyright: © 2026 by the authors. Licensee MDPI, Basel, Switzerland. This article is an open access article distributed under the terms and conditions of the Creative Commons Attribution (CC BY) license.

1. Introduction

1.1. Background

Arctic isolated microgrids supply electricity and heat to remote communities and industrial facilities that are not connected to centralized power grids. In northern Canada, these systems remain heavily dependent on diesel generators because harsh climatic conditions, limited site accessibility, complex fuel transportation logistics, and the need for a reliable year-round power supply constrain renewable energy integration [1,2]. Consequently, improving the efficiency and environmental performance of diesel generators remains essential to hybrid energy system development in remote Arctic regions.

Raglan Mine, located in Nunavik, Québec, represents a well-documented example of an Arctic mining microgrid where wind–diesel hybridization has been investigated to reduce diesel dependency [3]. Previous studies on Raglan Mine and similar remote mining operations show that, despite abundant wind resources, diesel generation continues to dominate system operation because of its dispatchability and reliability. The associated fuel transportation costs, greenhouse gas emissions, and operating expenses therefore remain significant challenges, highlighting the need to increase renewable energy utilization while improving diesel generator performance [4,5]. In this context, optimizing diesel engine calibration offers a practical, cost-effective way to reduce fuel consumption and engine-out emissions while improving operational efficiency without major modifications to the existing generation infrastructure.

Among the various retrofit strategies proposed for diesel generators, pneumatic hybridization offers a particularly attractive solution for hybrid microgrids operating under Arctic conditions. The concept enables independent control of the cylinder air charge by injecting compressed air into the engine intake manifold. An electrically driven compressor uses surplus wind-generated electricity to produce compressed air, stores it in a pressure vessel or underground cavern, and supplies it to the engine when needed [6,7]. By increasing the intake-air charge, pneumatic hybridization improves combustion thermodynamics and enables independent control of the compressor pressure ratio (PR_C), thereby enhancing engine flexibility and facilitating integration with renewable energy resources. Figure 1 illustrates the pneumatic hybridization concept together with its integration into the in-cylinder optimization framework developed in this study.

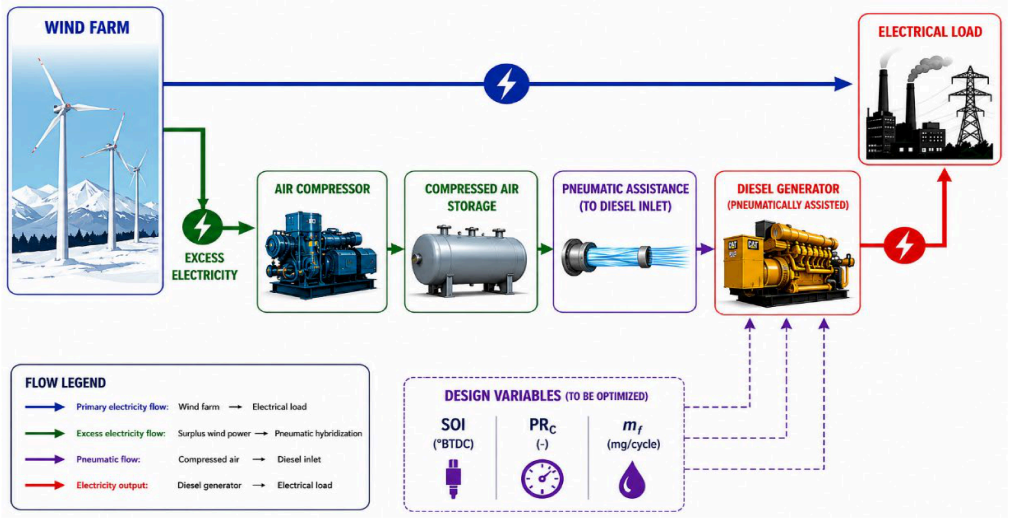

Figure 1. Pneumatic hybridization concept for Arctic diesel generators. This figure was prepared by the authors with graphical assistance from ChatGPT (GPT-6,OpenAI).

Ambient operating conditions strongly influence engine performance. In Arctic environments (T = 263 K, p = 0.943 bar), lower ambient temperatures increase intake-air density, partially compensating for the reduction in atmospheric pressure associated with altitude. These conditions directly affect cylinder filling, combustion efficiency, fuel consumption, and pollutant formation [8]. Consequently, engine calibration should be optimized under representative Arctic operating conditions.

Engine calibration is inherently a multi-objective optimization problem because simultaneous adjustments of design variables, including compressor pressure ratio, fuel injection timing, and injected fuel mass per cycle, directly influence brake power, brake-specific fuel consumption (BSFC), and NO_x emissions [9]. Improvements in one performance objective generally come with compromises in another, making the identification of balanced operating conditions a complex optimization task.

Exploring the full design space requires evaluating many candidate solutions, especially when global sensitivity analysis and multi-objective optimization are performed simultaneously. Directly coupling these algorithms with high-fidelity engine simulations is computationally prohibitive because it requires many function evaluations. Surrogate modeling offers an effective alternative by accurately approximating the nonlinear relationship between engine design variables and performance indicators using a limited number of high-fidelity simulations, dramatically reducing optimization cost while preserving predictive accuracy [10,11].

1.2. State of the Art

1.2.1. Arctic Isolated Microgrids and Diesel Generator Optimization

Many Arctic and subarctic communities and remote mining operations rely on isolated diesel-powered microgrids for electricity and heat. Connecting these systems to centralized electricity grids is generally neither technically nor economically feasible [12]. These microgrids operate under extreme climatic conditions while facing logistical challenges, high diesel transportation and storage costs, and geographic isolation. Consequently, many remote Canadian communities continue to rely heavily on stationary diesel generators for electricity and heating [1,4]. Considerable research has therefore focused on the design and optimization of hybrid renewable energy systems (HRESs) incorporating wind turbines, battery energy storage systems, photovoltaic systems, and other renewable technologies to reduce fuel consumption, minimize the levelized cost of energy (LCOE), and mitigate the environmental risks associated with diesel transportation and fuel spills [13–15]. An early study [16] demonstrated that adding wind turbines to an existing diesel power system serving an Alaskan village reduced diesel fuel consumption by approximately 50% while lowering annual operating costs by about 30%.

Several studies have contributed significantly to Arctic microgrid design and operation, but they typically model diesel generators using simplified steady-state performance models based on manufacturer heat-rate or fuel-consumption curves [17–20]. While this level of modeling is appropriate for system-level planning, it cannot capture the in-cylinder processes governing combustion and engine performance, including the effects of injection timing on NO_x formation, compressor pressure ratio on trapped air charge, and fuel mass per cycle on brake thermal efficiency under Arctic operating conditions. Consequently, although simplified diesel generator models are appropriate for system-level studies, they provide limited insight into engine behavior. As a result, opportunities to improve engine efficiency and reduce emissions through engine-level calibration remain largely unexplored.

1.2.2. Thermodynamic Simulation of Diesel Engines Using Diesel-RK

High-fidelity thermodynamic simulation plays a fundamental role in surrogate-assisted diesel engine calibration by generating physically consistent performance and emission data over a wide operating envelope [21]. Compared with simplified empirical engine models, physics-based simulation captures the complex interactions among combustion, heat transfer, gas exchange, and fuel injection, thereby providing a reliable basis for optimization studies.

Among one-dimensional engine simulation tools, the Diesel Razleytsev –Kuleshov (Diesel-RK) model [22] has become one of the most extensively validated platforms for full-cycle thermodynamic analysis of compression-ignition engines. Numerous studies have demonstrated its ability to accurately predict engine performance and emissions across a broad range of engine configurations, fuel types, and operating conditions [23–25].

Researchers have verified Diesel-RK's predictive capability by comparing it with experimental measurements for conventional diesel fuels, as well as biodiesel and alternative fuel blends. Validation studies generally report good agreement between simulated and experimental engine performance and emission characteristics, with prediction errors typically below approximately 5–7% for major parameters such as brake-specific fuel consumption, NO_x emissions, and combustion performance [24,26,27]. Diesel-RK has also been successfully applied to investigate the effects of operating parameters, including compression ratio, injection timing, and fuel properties, on engine efficiency and emissions, demonstrating its suitability as a high-fidelity simulation tool for engine calibration and optimization [27,28].

Despite this extensive validation, the application of Diesel-RK to pneumatically hybridized stationary diesel generators supplied from compressed air energy storage (CAES) systems remains limited [29,30]. Existing studies have focused primarily on conventional diesel engines or alternative fuels, with comparatively little attention to intake-air pressurization enabled by pneumatic hybridization. Furthermore, few investigations have integrated Diesel-RK with surrogate modeling and deterministic multi-objective optimization to calibrate large stationary diesel generators operating under representative Arctic conditions. This gap strongly motivates the unified computational framework proposed in the present study.

1.2.3. Pneumatic Hybridization of Diesel Generators

Pneumatic hybridization has emerged as a promising strategy for improving the performance of hybrid renewable energy systems operating in remote Arctic regions. The concept uses surplus electricity from renewable energy sources, particularly wind turbines, to compress and store air, then injects it into the diesel engine intake manifold to improve combustion and reduce fuel consumption [31]. By coupling compressed air energy storage (CAES) with conventional diesel generation, pneumatic hybridization provides an effective way to increase renewable energy utilization while maintaining the reliability required for isolated microgrids.

Early research established the engineering feasibility of pneumatic hybridization as an enabling technology for wind–diesel hybrid energy systems by integrating compressed air energy storage (CAES) with conventional diesel generation [32–35]. Initial investigations demonstrated the feasibility of integrating CAES into standalone wind–diesel systems and showed that appropriately sized compressed air storage can substantially increase wind energy penetration while reducing diesel fuel consumption [34]. Subsequent studies investigated the thermodynamic effects of intake-air pressure, intake temperature, and exhaust pressure on diesel engine operation, identifying operating conditions that improve combustion efficiency and minimize fuel consumption [31].

More recent developments have extended pneumatic hybridization from component-level investigations to integrated hybrid energy systems. Using measured wind data from Tuktoyaktuk in Northern Canada, Saad et al. [36] showed that hydro-pneumatic energy storage can significantly increase renewable energy utilization while maintaining a reliable electricity supply, achieving diesel fuel savings of up to 60% with renewable energy contributing approximately 70% of annual electricity production. Similarly, Martinez et al. [37] developed and validated a comprehensive wind–diesel–CAES simulation framework, benchmarked against HOMER, to quantify the effects of pneumatic hybridization on generator operating time, fuel consumption, and energy dissipation, thereby providing valuable guidance for system-level optimization.

Collectively, these studies established the technical feasibility and operational benefits of pneumatic hybridization as an enabling technology for hybrid renewable energy systems in remote Arctic applications. However, most investigations have focused on system-level performance using simplified thermodynamic cycle models or idealized engine representations. Consequently, the potential for optimizing the diesel generator itself through high-fidelity engine calibration has received comparatively little attention. Furthermore, pneumatic hybridization has rarely been investigated within a unified computational framework integrating high-fidelity engine simulation, surrogate modeling, global sensitivity analysis, deterministic multi-objective optimization, and objective multicriteria decision-making under representative Arctic operating conditions.

1.2.4. Surrogate-Assisted Multi-Objective Optimization of Diesel Generators

Surrogate-assisted optimization has become an effective approach for addressing computationally intensive engineering design problems by replacing expensive high-fidelity simulations with computationally efficient approximation models [38]. In diesel engine calibration, surrogate models establish the relationship between engine calibration parameters and performance indicators, enabling rapid exploration of the design space while substantially reducing computational cost. In this study, the design variables include the start of injection (SOI), compressor pressure ratio (PRc), and fuel mass per cycle (m_f), while the performance indicators include brake power, brake-specific fuel consumption (BSFC), peak cylinder pressure, and NO_x emissions.

The predictive capability of a surrogate model depends strongly on the quality and representativeness of the training dataset, making the design of experiments (DoE) a critical step in the calibration process [21,39]. Various sampling strategies have been proposed, including full and fractional factorial designs, central composite designs, Latin Hypercube Sampling (LHS), D-optimal designs, A-optimal designs, and Sobol low-discrepancy sequences. Among these methods, Sobol sampling has become particularly attractive for engine optimization because it provides a nearly uniform exploration of multidimensional design spaces while naturally supporting variance-based global sensitivity analysis [40,41]. Comparative studies show that Sobol sequences can achieve optimization results comparable to Latin Hypercube Sampling with substantially fewer simulation runs, improving computational efficiency without compromising solution quality [42].

Among surrogate modeling techniques, Gaussian Process (GP) models, also known as Kriging models, have become widely adopted for engineering optimization because they accurately approximate highly nonlinear response surfaces while estimating prediction uncertainty. Combined with efficient sampling strategies such as Sobol sequences, GP models can reproduce complex engine-response surfaces using relatively few high-fidelity simulations, significantly reducing the computational burden of multi-objective optimization [10,38].

Numerous studies have successfully applied surrogate-assisted optimization to diesel engine calibration. For example, a previous study [11] combined Kriging surrogate models with constrained multi-objective optimization to identify the trade-off between brake-specific fuel consumption and NO_x emissions using a high-fidelity GT-Power engine model. Their approach reduced calibration computational cost by more than 85% while accurately reproducing the Pareto-optimal solutions. More recently, machine-learning-based surrogate models have also demonstrated excellent predictive performance for combustion modeling, with advanced Long Short-Term Memory (LSTM) architectures outperforming transformer-based models in predicting ignition delay while maintaining high accuracy and low computational cost [43]. These studies highlight the growing importance of surrogate modeling for accelerating engine design and calibration.

Beyond computational efficiency, global sensitivity analysis (GSA) provides valuable physical insight into how calibration parameters influence engine performance and emissions. Variance-based Sobol sensitivity indices have been extensively employed to quantify the contribution of operating and design variables to combustion characteristics, fuel consumption, and pollutant formation [44]. Such analyses not only identify the most influential parameters but also reveal nonlinear interactions among calibration variables, thereby improving both the interpretability and robustness of optimization results. Similarly, multi-objective optimization studies have shown the importance of considering engine efficiency and pollutant emissions simultaneously, highlighting the inherent trade-offs in diesel engine calibration [45].

Despite these significant advances, most published studies address design of experiments, surrogate modeling, global sensitivity analysis, and multi-objective optimization as independent tasks. Few investigations have integrated these complementary methodologies into a unified computational framework that combines high-fidelity engine simulation, efficient surrogate modeling, sensitivity analysis, and deterministic multi-objective optimization. Furthermore, applications to pneumatically hybridized stationary diesel generators operating under representative Arctic conditions remain extremely limited, providing the principal motivation for the methodology developed in the present study.

1.2.5. Decision-Making on the Pareto Front

Multi-objective optimization produces a set of Pareto-optimal solutions rather than a single optimal operating point. Consequently, selecting the most appropriate solution for practical implementation requires an additional decision-making step that balances competing performance criteria while preserving the trade-offs identified during optimization. This final stage is particularly important for diesel engine calibration, where improvements in fuel consumption, engine performance, and pollutant emissions are inherently conflicting objectives.

Several multicriteria decision-making (MCDM) methods have been proposed to rank Pareto-optimal solutions, including weighted-sum approaches and the Technique for Order Preference by Similarity to Ideal Solution (TOPSIS) [46,47]. Although these methods have been successfully applied to engineering optimization problems, many require predefined weighting factors or decision-maker preferences, introducing subjectivity that can influence the final ranking and reduce the reproducibility of the decision-making process [48].

An alternative is the Sequential Interactive Modeling for Urban Systems (SIMUS) method, introduced in [48] which ranks Pareto-optimal solutions through sequential linear programming without requiring predefined weighting factors. By eliminating subjective preference weights, SIMUS provides a transparent, objective, and reproducible framework for identifying the most appropriate engineering solution while preserving the compromise among competing objectives. Basakayi et al. [49] recently demonstrated its applicability

to energy systems by applying SIMUS to select and rank energy storage technologies. Different MCDM methods may produce different rankings even when applied to the same alternatives and criteria (the same initial decision matrix). This behavior is also reported in [49], where SIMUS, TOPSIS, and VIKOR agreed on the leading alternatives while differing in the ranking of several intermediate alternatives.

Although considerable progress has been achieved in surrogate-assisted optimization, multicriteria decision-making, and high-fidelity engine simulation, these methodologies have generally been developed and applied independently. Consequently, the literature largely lacks an integrated decision-support framework that combines high-fidelity thermodynamic simulation, surrogate modeling, global sensitivity analysis, deterministic multi-objective optimization, and objective Pareto ranking, particularly for pneumatically hybridized diesel generators operating under representative Arctic conditions. This study addresses this gap as its principal contribution.

In this study, we investigate pneumatic hybridization at the engine level, treating compressed air as an externally available energy input; we do not include compressed air generation, storage, and distribution in the optimization.

1.2.6. Research Gap

The literature demonstrates substantial progress in hybrid energy systems for Arctic microgrids, high-fidelity diesel engine simulation, pneumatic hybridization, surrogate-assisted optimization, and multicriteria decision-making. However, these developments have largely evolved independently. Existing studies either optimize hybrid energy systems using simplified diesel generator models or investigate engine calibration without considering the broader hybrid system context. Furthermore, few studies integrate high-fidelity Diesel-RK simulations, surrogate modeling, Sobol-based global sensitivity analysis, deterministic multi-objective optimization, and objective Pareto ranking within a unified computational framework. This limitation is particularly evident for pneumatically hybridized stationary diesel generators operating under representative Arctic conditions, motivating the methodology proposed here.

Each stage of the proposed framework addresses a specific methodological limitation. High-fidelity Diesel-RK simulation provides the physical database but is computationally expensive for direct multi-objective exploration; adaptive sampling and Gaussian Process modeling therefore reduce this computational burden while quantifying predictive uncertainty; Sobol analysis provides physical interpretation of the relationships captured by the surrogates while mechanical and convex-hull constraints restrict optimization to physically admissible and data-supported regions. Multi-objective optimization reduces dependence on a single search strategy, and SIMUS provides a systematic way to select a compromise from the resulting non-dominated alternatives. Finally, the selected solution is returned to Diesel-RK for independent high-fidelity confirmation, as surrogate accuracy varies across objectives. The framework's distinctive advantage, therefore, lies in the closed-loop integration of these complementary stages, linking physical modeling, computational efficiency, physical interpretation, constrained optimization, decision-making, and high-fidelity confirmation into a single verification workflow.

1.3. Research Contributions

Building on the research gaps identified in Section 1.2, this study's main methodological contribution is an integrated, physically constrained, and uncertainty-aware calibration framework. More specifically, the study makes the following contributions:

- Develops a unified surrogate-assisted calibration framework that integrates high-fidelity Diesel-RK thermodynamic simulations, adaptive Sobol design of experiments

with targeted post-validation resampling, Gaussian Process (GP) surrogate modeling, Sobol global sensitivity analysis, deterministic multi-objective optimization, SIMUS-based Pareto decision-making, and high-fidelity validation within a single computational workflow.

- Extends the calibration of pneumatically hybridized stationary diesel generators by simultaneously optimizing three key engine-control variables: start of injection (SOI), compressor pressure ratio (PR_C), and fuel mass per cycle (m_f), under representative Arctic operating conditions, thereby strengthening the integration of engine-level optimization within hybrid renewable energy systems.
- Demonstrates that Gaussian Process surrogate models can accurately reproduce high-fidelity Diesel-RK predictions for brake power, brake-specific fuel consumption, peak cylinder pressure, and NO_x emissions while explicitly quantifying predictive uncertainty, enabling computationally efficient and reliable multi-objective optimization.
- Introduces a physically constrained optimization framework that combines mechanical operating limits with convex-hull domain membership to ensure physically meaningful surrogate predictions. The necessity of these constraints is demonstrated through both surrogate-based and direct high-fidelity optimization, showing that they improve solution robustness rather than serving as merely precautionary safeguards.
- Establishes an uncertainty-aware validation methodology that propagates Gaussian Process predictive uncertainty throughout the calibration process, including parity analysis, response-surface characterization, Pareto-front construction, and final operating-point selection. The proposed framework is validated using a CAT 3516 stationary diesel generator, with the selected calibration point lying within the surrogate's 95% predictive interval for all optimized objectives.

Collectively, these contributions provide an integrated computational framework for high-fidelity calibration of pneumatically hybridized diesel generators, advancing surrogate-assisted optimization for hybrid energy systems operating under demanding Arctic conditions.

1.4. Organization of the Paper

The remainder of this paper is organized as follows. Section 2 presents the proposed methodology, including the Diesel-RK thermodynamic model, the pneumatic hybridization concept, the Arctic operating conditions, the adaptive design of experiments, Gaussian Process surrogate modeling, global sensitivity analysis, deterministic multi-objective optimization, and the SIMUS-based decision-making framework. Section 3 presents the results, including surrogate model validation, response surface analysis, global sensitivity analysis, multi-objective optimization, Pareto-front evaluation, multicriteria decision-making, and high-fidelity Diesel-RK verification. Section 4 discusses the engineering implications of the proposed framework, the role of predictive uncertainty in surrogate-assisted optimization, the benefits of tri-objective optimization for diesel engine calibration, and the limitations of the proposed methodology. Finally, Section 5 summarizes the principal findings, highlights the study's main contributions, and outlines directions for future research.

1.5. Relationship with Previous Conference Publication

This manuscript substantially extends the conference paper presented at the MDPI-IOCEN 2026 Conference [50]. The conference paper introduced the general concept of surrogate-assisted optimization for pneumatically hybridized diesel generators, whereas the present journal article significantly expands both the scope and the scientific contributions of the work. The principal extensions include:

- A comprehensive review of the literature on Arctic hybrid energy systems, pneumatic hybridization, surrogate-assisted optimization, and multicriteria decision-making;
- A detailed high-fidelity Diesel-RK thermodynamic model of the pneumatically hybridized diesel generator;
- An adaptive Sobol design of experiments incorporating targeted post-validation resampling;
- Gaussian Process surrogate modeling with explicit predictive uncertainty quantification;
- Sobol-based global sensitivity analysis to identify the relative influence of engine calibration parameters;
- Deterministic tri-objective optimization considering engine performance, fuel consumption, and emissions;
- Objective Pareto-front ranking using the SIMUS multicriteria decision-making method;
- Comprehensive surrogate and high-fidelity model validation; and
- An expanded discussion of the engineering implications, methodological limitations, and practical applications for Arctic hybrid energy systems.

Consequently, the present manuscript represents a substantial methodological and scientific advancement over the conference publication and provides a complete, validated framework for surrogate-assisted calibration of pneumatically hybridized diesel generators operating under representative Arctic conditions.

2. Methodology

The proposed methodology is summarized in the integrated computational framework shown in Figure 2. The framework consists of five sequential stages: (1) problem definition and system characterization, (2) high-fidelity thermodynamic modeling using Diesel-RK, (3) adaptive dataset construction and Gaussian Process surrogate modeling, (4) surrogate-assisted multi-objective optimization, and (5) objective decision-making followed by high-fidelity validation of the selected solution. The following subsections describe each stage of the proposed framework in detail.

As shown in Figure 2, the methodology begins by defining the case study, modeling assumptions, decision variables, objectives, and constraints that establish the optimization problem addressed throughout this work.

2.1. Problem Definition and Case Study

2.1.1. Case Study

The proposed methodology is demonstrated using the CAT 3516 stationary diesel generator at Raglan Mine, an isolated mining facility in Nunavik, Québec, Canada (61° N), operated by Glencore. Raglan Mine provides a representative case study of an Arctic hybrid microgrid, where diesel generation remains essential to ensure a reliable electricity supply, despite the availability of renewable energy resources.

The CAT 3516 is a turbocharged V-16, four-stroke diesel engine operating at a constant speed of 1800 rpm. The engine has a bore of 170 mm, a stroke of 190 mm, a compression ratio of 13:1, and a rated brake power of 1492 kW under SAE J1995 [51] reference conditions (T = 298 K, p = 0.99 bar). These engine specifications provide the basis for the high-fidelity Diesel-RK simulations performed throughout this study.

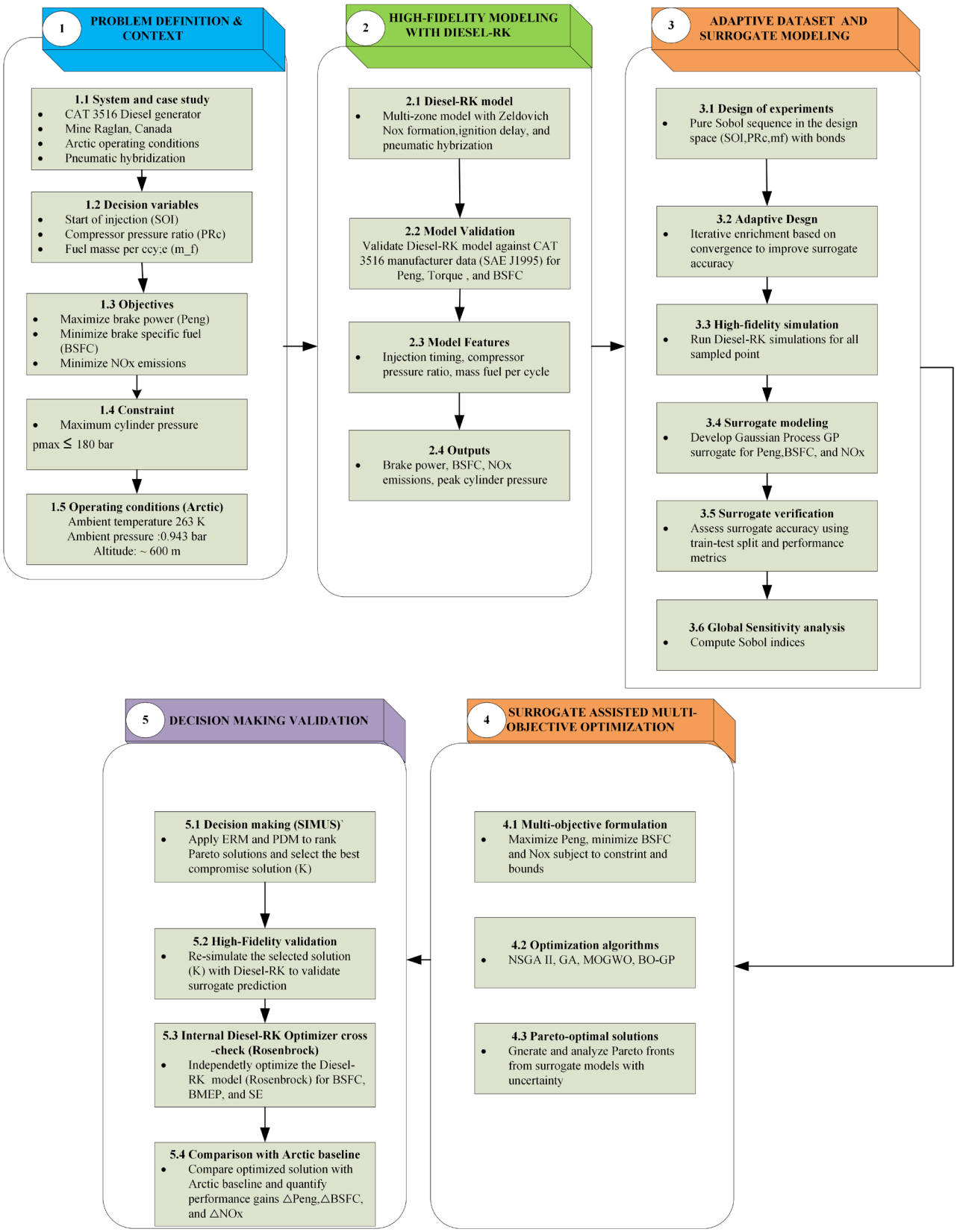

Figure 2. Overall methodological framework of the proposed surrogate-assisted optimization approach.

2.1.2. Scope and Modeling Assumptions

The present work focuses exclusively on optimizing pneumatic hybridization at the engine calibration level, considering fuel delivery and in-cylinder combustion processes.

This study excludes the design and sizing of the hybrid energy system, including wind turbines, air compressors, compressed air energy storage (CAES), and compressed air distribution; these will be addressed in future work.

Accordingly, we assume compressed air is available on demand, and we represent its influence on engine operation by the compressor pressure ratio (PR_C), one of the engine calibration variables. The analysis is conducted under representative Arctic operating conditions corresponding to Raglan Mine, with an ambient temperature of 263 K, an atmospheric pressure of 0.943 bar, and an altitude of approximately 600 m above sea level. Consequently, in this study, pneumatic hybridization refers specifically to engine-level operation with externally available compressed air assistance within the overall architecture shown in Figure 1, which includes the wind turbine, compressed air system, and diesel engine. The present optimization is restricted to the engine-level design variables PRc, SOI, and m_f, where PRc represents the imposed level of compressed air assistance. The optimized engine calibration is intended for operating periods during which compressed air is available from the external storage system, while conventional engine operation applies when pneumatic assistance is unavailable. The complete pneumatic energy chain is neither modeled nor optimized in the present study. In particular, compressed air generation, storage, and distribution, including their associated energy requirements, fall outside the present scope and will be addressed in future system-level work.

2.1.3. Optimization Problem Formulation

Engine calibration is formulated as a deterministic tri-objective optimization problem involving three decision variables:

- Start of injection: SOI $\in [6°, 20°]$ BTDC;
- Compressor pressure ratio: $PR_C \in [1.5, 4.0]$;
- Fuel mass per cycle: $m_f \in [0.25, 0.385]$ g/cycle.

The optimization simultaneously seeks to:

- Maximize brake power (P_{eng});
- Minimize brake-specific fuel consumption (BSFC);
- Minimize engine-out NO_x emissions.

Candidate solutions must satisfy two feasibility criteria applied during the optimization process (Section 2.4.2):

1. The maximum cylinder pressure must satisfy $p_{max} \leq 180$ bar, which represents a conservative mechanical operating limit [9], although modern heavy-duty diesel engines may operate at peak cylinder pressures exceeding 230 bar [8];
2. The candidate solution must remain within the convex hull of the surrogate model training dataset, ensuring that optimization is restricted to the region supported by high-fidelity simulation data and avoiding unreliable surrogate extrapolation.

2.2. High-Fidelity Engine Model

High-fidelity engine simulations were performed using Diesel-RK (version 4.3.0.189), a one-dimensional thermodynamic engine simulation software based on the RK multi-zone combustion model [22]. Originally developed by Razleytsev and subsequently extended by Kuleshov, the model predicts in-cylinder combustion processes using a multi-zone formulation, thermal NO_x formation through the extended Zeldovich mechanism, and ignition delay using the Tolstov correlation. These physically based models provide the predictive capability required for accurate engine calibration and surrogate model development.

Pneumatic hybridization was represented by supplying compressed air from a Compressed Air Energy Storage (CAES) system to the engine intake manifold. The influence

of pneumatic assistance was modeled through the compressor pressure ratio (PR_C), introduced as an independent engine calibration variable alongside the start of injection (SOI) and the fuel mass per cycle (m_f). This formulation enables the direct assessment of pneumatic hybridization on combustion, engine performance, fuel consumption, and NO_x emissions while remaining consistent with the proposed optimization framework.

The Diesel-RK model was configured according to the manufacturer's specifications for the CAT 3516 stationary diesel generator. The principal engine geometry, operating conditions, and simulation parameters are summarized in Table 1.

Table 1. Diesel-RK configuration parameters for the CAT 3516 engine.

Parameter	Value
Bore/Stroke	170 mm/190 mm
Compression ratio	13:1
Number of cylinders	16
Engine speed	1800 rpm
Displacement	69.06 L
Aspiration	Turbocharged/Aftercooled
Compressor adiabatic efficiency η_C	0.84
Intake pressure loss Δp_{in}	0.02 bar
Exhaust back pressure Δp_{out}	0.04 bar
Intake/Exhaust valve diameter	55.2 mm/53.7 mm

The model was first validated against the manufacturer's performance data for the CAT 3516 engine over the operating range of 1350–1800 rpm under SAE J1995 reference conditions, as presented in Section 3.1. Following validation, the calibrated model was evaluated under representative Arctic operating conditions by modifying the ambient temperature and atmospheric pressure while maintaining the validated engine and turbocharger calibration parameters. The resulting Arctic reference case serves as the baseline for the surrogate-assisted optimization presented in the following sections and is reported in Section 3.1.

The compressed air thermodynamic assumptions are as follows: the compressor inlet state was defined by representative Arctic ambient conditions (T_{amb} = 263 K and p_{amb} = 0.943 bar), with an adiabatic compressor efficiency of η_C = 0.84. Charge-air cooling was modeled in Diesel-RK using an intercooler with a constant effectiveness of E_{cool} = 0.75 and a pressure loss of 0.05 bar. The intercooler coolant temperature was assumed equal to the ambient temperature ($T_{cool} = T_{amb}$ = 263 K). Consequently, the compressed air temperature was calculated internally by Diesel-RK for each compressor operating condition. For example, at PR_c = 3.721, Diesel-RK reports a post-intercooler temperature of 311.99 K (38.84 °C) and a corresponding pressure of 3.4145 bar.

2.3. Adaptive Surrogate Construction

2.3.1. Database Generation

A Sobol low-discrepancy sequence was adopted as the design of experiments (DoE) to sample the three-dimensional calibration space defined by the fuel mass per cycle (m_f), compressor pressure ratio (PR_C), and start of injection (SOI). Because the predictive capability of surrogate models depends strongly on the quality and representativeness of the training dataset, the database was generated through an adaptive sampling strategy rather than a single, fixed sampling campaign [52].

The initial database was constructed progressively using successive Sobol sampling stages. At each stage, convergence was evaluated using two complementary criteria: (i) the uniformity of the sampling distribution, quantified through the Centered Discrepancy (CD) metric, and (ii) the predictive performance of the corresponding surrogate models, evaluated using the coefficient of determination (R^2) and the mean absolute percentage error (MAPE) on an independent test dataset. We introduced additional sampling only when these convergence indicators suggested further improvement in surrogate accuracy. Section 3.3 presents the evolution of these convergence metrics.

Following convergence of the initial Sobol design, additional high-fidelity Diesel-RK simulations were performed to evaluate candidate operating points identified during the optimization process (Section 2.5.2). Comparison between surrogate predictions and high-fidelity simulations revealed localized regions where the prediction error remained comparatively large. These regions were subsequently enriched using a targeted Latin Hypercube Sampling (LHS) strategy, concentrating new samples within the areas exhibiting the largest discrepancies. This two-stage adaptive strategy combines the excellent global space-filling properties of Sobol sequences with local refinement driven by high-fidelity model feedback, thereby improving surrogate accuracy while minimizing the number of expensive engine simulations. The final database size is reported in Section 3.3.

2.3.2. Gaussian Process Surrogate Models

Four independent Gaussian Process (GP) surrogate models were developed to predict brake power (P_{eng}), brake-specific fuel consumption (BSFC), engine-out NO_x emissions, and maximum cylinder pressure (p_{max}). Each model employed a Matérn 5/2 covariance kernel with Automatic Relevance Determination (ARD) together with an additive white-noise term, implemented using the GaussianProcessRegressor class of the scikit-learn library [53].

All surrogate models were trained using the complete enriched database described in Section 2.3.1. Importantly, no samples were excluded during surrogate construction. The mechanical constraint $p_{max} \leq 180$ bar was enforced only during the optimization stage (Section 2.4.2), allowing the pressure surrogate to learn the complete physical response of the engine rather than a pre-filtered subset of operating conditions.

Kernel hyperparameters were determined by maximizing the log-marginal likelihood, using multiple random restarts to reduce the likelihood of convergence toward local optima [53].

Gaussian Process (GP) regression was selected because it simultaneously provides a predictive mean and an associated predictive uncertainty for every operating point. This probabilistic formulation offers a significant advantage over deterministic surrogate models such as Random Forests or conventional feed-forward neural networks, whose predictions do not directly quantify confidence. In the proposed framework, GP uncertainty estimates are propagated throughout the optimization and validation procedures (Section 2.5.3), providing an objective criterion for distinguishing operating points that require confirmation through high-fidelity Diesel-RK simulations from those that can be accepted directly.

The overall surrogate-model development process is illustrated in Figure 3 [38].

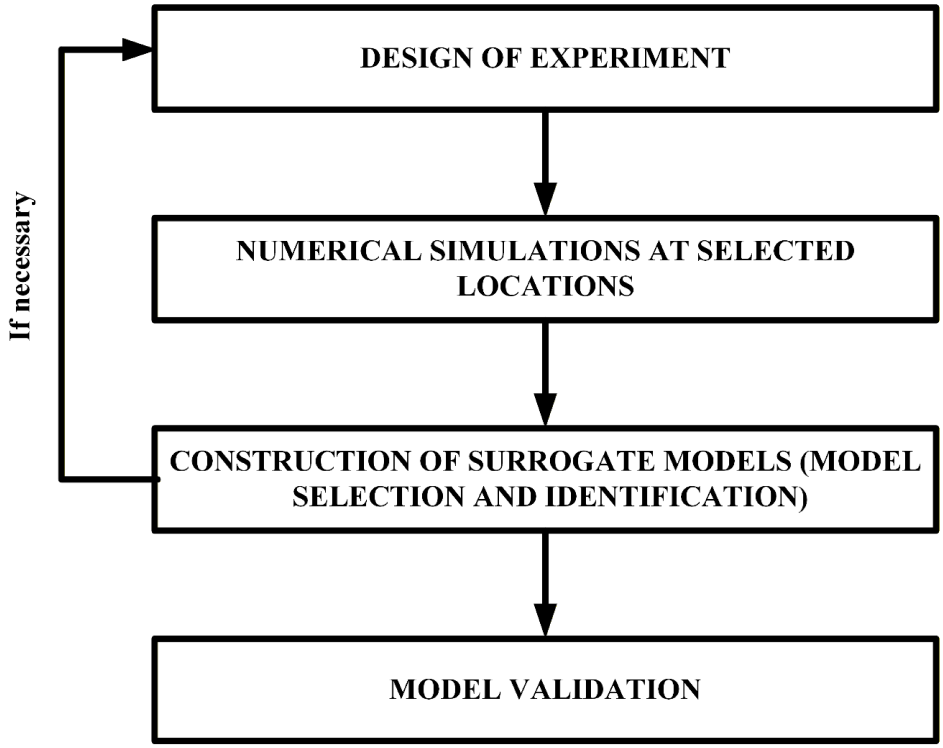

Figure 3. Flowchart of the surrogate modeling.

2.3.3. Surrogate Verification

This section concerns the verification of the Gaussian Process approximations against Diesel-RK-generated high-fidelity data and is distinct from the prior validation of the Diesel-RK engine model against reference engine data.

The predictive performance of the four Gaussian Process surrogate models was assessed using two complementary validation procedures.

First, leave-one-out cross-validation (LOO-CV) was employed to evaluate model generalization. Each surrogate was repeatedly trained using all but one sample, with the excluded sample subsequently used for validation. Repeating this process for the entire database provides a robust estimate of predictive accuracy while allowing the complete dataset to be retained for training the final surrogate models.

Second, a 80/20 holdout validation was performed using data not involved in either surrogate training or LOO-CV, thereby providing an assessment of predictive performance on previously unseen operating conditions.

Four complementary performance indicators were used to evaluate each surrogate:

- The coefficient of determination (R^2), which measures the overall goodness of fit;
- The root-mean-square error (RMSE), which quantifies the magnitude of prediction errors;
- The mean absolute percentage error (MAPE), providing a physically interpretable measure of relative prediction accuracy; and
- The 95% prediction-interval coverage, defined as the proportion of validation samples falling within ± 1.96 standard deviations of the Gaussian Process predictive mean.

We evaluated surrogate performance after completing the adaptive enrichment procedure described in Section 2.5.2. We applied leave-one-out validation and a random 80/20 holdout partition to the complete enriched dataset. Although the 20% holdout subset was excluded from the final surrogate fit used for performance reporting, it was drawn from a dataset whose composition had already been determined through adaptive enrichment. The reported results therefore quantify internal post-enrichment predictive performance

and coverage conditional on the adaptive enriched sampling distribution, not independent end-to-end uncertainty calibration.

Unlike conventional surrogate validation, the present framework evaluates not only prediction accuracy but also the statistical calibration of predictive uncertainty [38]. Reliable uncertainty estimates are essential because they support the uncertainty-aware validation strategy developed in this work (Section 4.1), including candidate-solution screening, Pareto-front analysis, and final high-fidelity confirmation. A surrogate exhibiting a high R^2 but poorly calibrated prediction intervals would therefore be unsuitable for the proposed optimization framework.

Section 3.4 presents the validation results for all four surrogate models.

2.4. Surrogate-Assisted Optimization

2.4.1. Global Sensitivity Analysis

We performed variance-based global sensitivity analysis (GSA) on the trained Gaussian Process surrogate models using the Saltelli sampling scheme and estimator implemented in SALib [54]. We computed first-order Sobol sensitivity indices (S_1), which quantify each design variable's contribution to output variance, and total-order indices (S_T), which also account for interactions among variables, independently for all four surrogate models over the full three-dimensional calibration domain.

The sensitivity analysis served two complementary purposes. First, it provided a physical interpretation of the surrogate models by identifying the relative influence of the engine calibration variables on brake power, brake-specific fuel consumption, peak cylinder pressure, and NO_x emissions. Second, it verified that the surrogate models reproduced physically meaningful relationships consistent with established diesel combustion behavior, thereby increasing confidence in their use for optimization. The resulting sensitivity indices also supported the interpretation of the optimal calibration strategy discussed in Section 4.2.

Section 3.6 presents the complete GSA results.

2.4.2. Multi-Objective Optimization

The engine calibration problem was formulated as a tri-objective optimization problem that maximizes brake power while minimizing brake-specific fuel consumption and engine-out NO_x emissions. Because no optimization algorithm is universally superior for all optimization problems, a consequence of the No Free Lunch theorem [55], four optimization algorithms representing complementary optimization paradigms were evaluated.

Surrogate modeling enables this comparison by replacing computationally expensive Diesel-RK simulations with Gaussian Process models during optimization. Because multi-objective optimization requires thousands of objective-function evaluations, surrogate models dramatically reduce computational cost while maintaining the predictive accuracy established during validation [38].

The following optimization algorithms were investigated:

- Non-dominated Sorting Genetic Algorithm II (NSGA-II). A widely used evolutionary algorithm based on non-dominated sorting, crowding-distance preservation, simulated binary crossover (SBX), and polynomial mutation [56–60];
- Classical Genetic Algorithm (GA). Implemented using tournament selection together with SBX crossover and polynomial mutation, where multiple optimization runs were performed using Dirichlet-sampled scalarization weights to approximate the Pareto front [61–63];
- Grey Wolf Optimizer (GWO). Implemented as a multi-objective variant employing an external archive of non-dominated solutions and feasibility-first constrained dominance to guide the search toward feasible Pareto-optimal regions [64–68];

- Bayesian Optimization using Gaussian Processes (BO-GP). Implemented as a sequential optimization strategy initialized through Latin Hypercube Sampling and guided by a Lower Confidence Bound (LCB) acquisition function to balance exploration of uncertain regions and exploitation of promising solutions [69,70].

Each optimization algorithm received a computational budget consistent with its search paradigm rather than an identical number of function evaluations. This strategy provides a more meaningful comparison by allowing each algorithm to operate under conditions representative of its intended application. Because this study evaluates the proposed surrogate-assisted optimization framework rather than statistically benchmarking stochastic optimization algorithms, each algorithm was executed once using the fixed random seed specified in Table 2. Fixed initialization conditions ensure full reproducibility of the reported results and enable a consistent comparison of fundamentally different optimization paradigms under identical computational conditions. The principal optimization parameters are summarized in Table 2.

Table 2. Optimization algorithm parameters.

Algorithm	Population/ Archive	Crossover/Mutation	Generations/Iteration	Seed	Other
NSGA-II	200	SBX (p = 0.90, η = 15)/PM (η = 20)	300	42	Native constraint handling (p_{max}, hull)
GA (classical)	20	SBX (p = 0.90, η = 15)/PM (η = 20)	20 generations × 20 Dirichlet weight vectors	1	Tournament selection
GWO	40 wolves	-	199	42	Archive cap 150, leaders drawn randomly from archive
BO-GP	10 initial (LHS):150 total	-	Sequential, 1 point/iteration	99	LCB acquisition, iterative meta-GP refit

2.4.3. Optimization Performance Assessment

We evaluated the relative performance of the four optimization algorithms using the three-dimensional hypervolume indicator, computed with the pymoo framework using a common reference point dominated by all Pareto-optimal solutions obtained during the study.

The hypervolume indicator was selected because it simultaneously measures two essential characteristics of multi-objective optimization performance: convergence toward the true Pareto front and diversity of the obtained solutions. Unlike metrics that evaluate only the quality of individual solutions, the hypervolume provides a comprehensive assessment of an algorithm's ability to generate a well-distributed approximation of the Pareto front.

Section 3.7 presents the optimization performance results.

2.5. Solution Selection and High-Fidelity Validation

2.5.1. Multicriteria Decision-Making

The four optimization algorithms generated non-dominated solutions, which were merged into a single combined Pareto front, from which a single operating point was selected using the Sequential Interactive Modeling for Urban Systems (SIMUS) method. Unlike conventional multicriteria decision-making (MCDM) approaches that rely on pre-

defined weights or user-defined preferences, SIMUS provides an objective, reproducible ranking of Pareto-optimal solutions through sequential linear programming, preserving the trade-offs identified during multi-objective optimization [48,49].

To ensure the final decision represented the entire Pareto front, we selected eleven representative operating points by sorting the non-dominated solutions by brake power and sampling evenly across the resulting range. For each alternative, we constructed an Efficient Results Matrix (ERM) by solving three sequential linear programming problems corresponding to the three optimization objectives: maximizing brake power, minimizing brake-specific fuel consumption, and minimizing engine-out NO_x emissions, while maintaining the remaining objectives at or better than their average values.

SIMUS conventionally defines the right -hand-side (RHS) constraints from the criterion extrema [48]. However, applying this convention to the present decision matrix resulted in an infeasible formulation because the individual criterion extrema could not be satisfied simultaneously. Therefore, we adopted the mean value of each criterion as its RHS. This choice is consistent with [48], which allows the decision-maker to specify the RHS values.

SIMUS then ranked the alternatives using two independent procedures derived from the same ERM: Procedure 1, based on normalized ERM scores, and Procedure 2, based on the Project Dominance Matrix (PDM), which establishes pairwise dominance relationships among the alternatives. Agreement between the two rankings provides an internal consistency check and further strengthens the objectivity and reproducibility of the final operating-point selection. The highest-ranked solution was retained as the recommended engine calibration.

2.5.2. High-Fidelity Validation

The operating point selected by the SIMUS procedure was independently re-evaluated using the high-fidelity Diesel-RK thermodynamic model under the same Arctic operating conditions used throughout surrogate development. This validation step provides an independent assessment of the surrogate-assisted optimization framework because it verifies the final solution directly using the underlying physics-based engine model rather than the surrogate approximation [22,71].

We compared surrogate predictions for brake power, brake-specific fuel consumption, and engine-out NO_x emissions with the corresponding Diesel-RK results using two complementary performance measures. First, the relative percentage error quantified the agreement between surrogate and high-fidelity predictions. Second, the prediction error was normalized by the Gaussian Process predictive standard deviation, providing an uncertainty-aware validation criterion. A prediction within ± 1.96 predictive standard deviations indicates that the observed error is consistent with the surrogate's estimated uncertainty, confirming not only prediction accuracy but also the statistical calibration of the uncertainty model.

Section 3.9 presents the validation results. During the optimization-validation loop, we evaluated selected optimization candidates with the high-fidelity Diesel-RK model. We added candidate points with significant discrepancies between surrogate predictions and high-fidelity responses to the dataset, then updated the surrogate before continuing the optimization process. Leave-one-out validation and the 80/20 holdout evaluation were performed only after the complete enriched dataset had been assembled, as described in Section 2.3.3.

2.5.3. Internal Diesel-RK Optimizer Cross-Check

To further assess the robustness of the proposed methodology, we performed an additional optimization using the native Diesel-RK optimizer, providing a completely

independent reference that does not rely on surrogate modeling. The built-in optimizer uses the Rosenbrock direct-search algorithm and operates directly on the physical combustion model, allowing comparison of the surrogate-assisted framework with a conventional high-fidelity optimization approach.

We investigated three objective functions available in Diesel-RK independently: minimizing specific fuel consumption (SFC), maximizing brake mean effective pressure (BMEP), and minimizing the composite emission index (SE). SE is defined in Diesel-RK as

$$\mathrm{SE} = \frac{C_{\mathrm{pm}}\,\mathrm{PM}}{0.15} + \frac{C_{\mathrm{NO}}\,\mathrm{NO_x}}{7},$$

where PM and NO_x denote particulate matter and nitrogen oxide emissions, respectively, and C_{pm} = 0.5 and C_{NO} = 1.0 are weighting coefficients.

For all three optimization problems, the start of injection (SOI) and compressor pressure ratio (PR_C) were treated as decision variables, while the fuel mass per cycle was fixed at its Arctic baseline value (m_f = 0.3628 g/cycle). The optimization enforced the maximum cylinder pressure constraint throughout the process.

We then evaluated the optimal calibration parameters for each objective function using a complete Diesel-RK simulation to determine the corresponding brake power, brake-specific fuel consumption, and NO_x emissions. This independent optimization provides two complementary forms of validation. First, it establishes a physically based benchmark for comparison with the surrogate-assisted multi-objective optimization results. Second, it evaluates the practical necessity of the convex-hull constraint introduced in Section 2.4.2 by examining whether unconstrained high-fidelity optimization converges toward operating points outside the domain represented by the surrogate training data. The corresponding results are discussed in Sections 3.9 and 4.4.

3. Results

3.1. Diesel-RK Model Validation and Arctic Baseline

The high-fidelity Diesel-RK model was validated against the manufacturer's CAT 3516 performance data (Appendix A) under SAE J1995 reference conditions (T = 298 K, p = 0.99 bar) over the engine operating range of 1350–1800 rpm. Figures 4–6 compare the simulated brake power, brake torque, and brake-specific fuel consumption (BSFC) with the corresponding manufacturer performance curves.

Maximum deviations of 1.36% for brake power, 1.35% for brake torque, and 5.9% for BSFC were obtained, while the corresponding mean absolute errors were 0.88%, 0.90%, and 2.25%, respectively. The slightly larger deviation observed for BSFC is expected because this quantity is derived from both fuel flow rate and brake power, making it more sensitive to small discrepancies in the underlying thermodynamic predictions. The validation errors are well within the accuracy generally reported for high-fidelity Diesel-RK simulations in the literature (see Section 1.2.2).

These results show excellent agreement between the numerical model and the manufacturer's performance data, confirming that the Diesel-RK model accurately reproduces engine behavior across its full operating range. The validated model therefore provides a reliable high-fidelity reference for the surrogate-assisted optimization framework developed in this study.

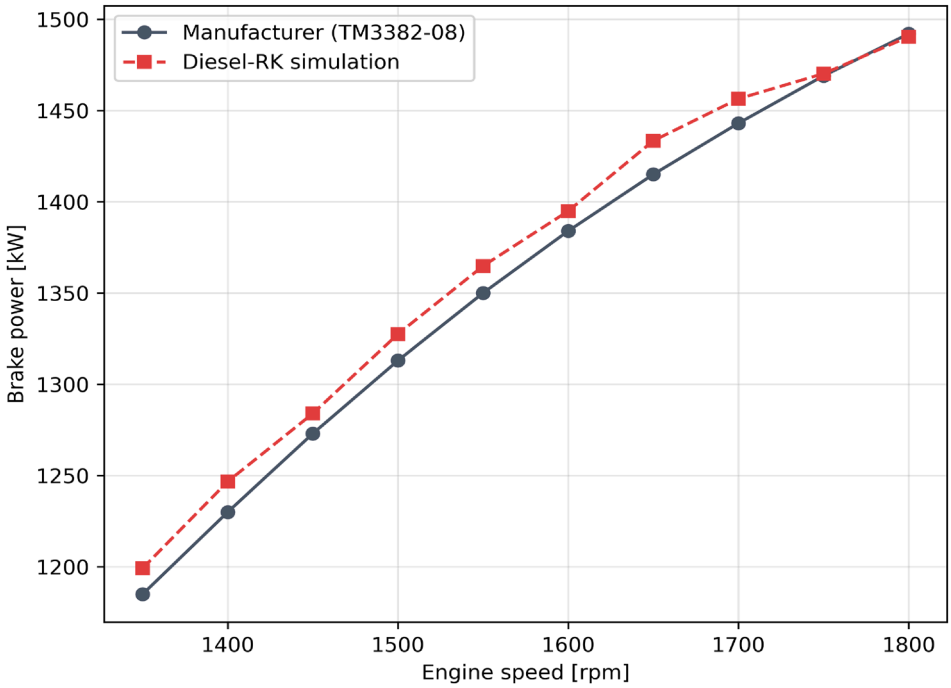

Figure 4. Brake power as a function of engine speed: Diesel-RK predictions versus manufacturer data.

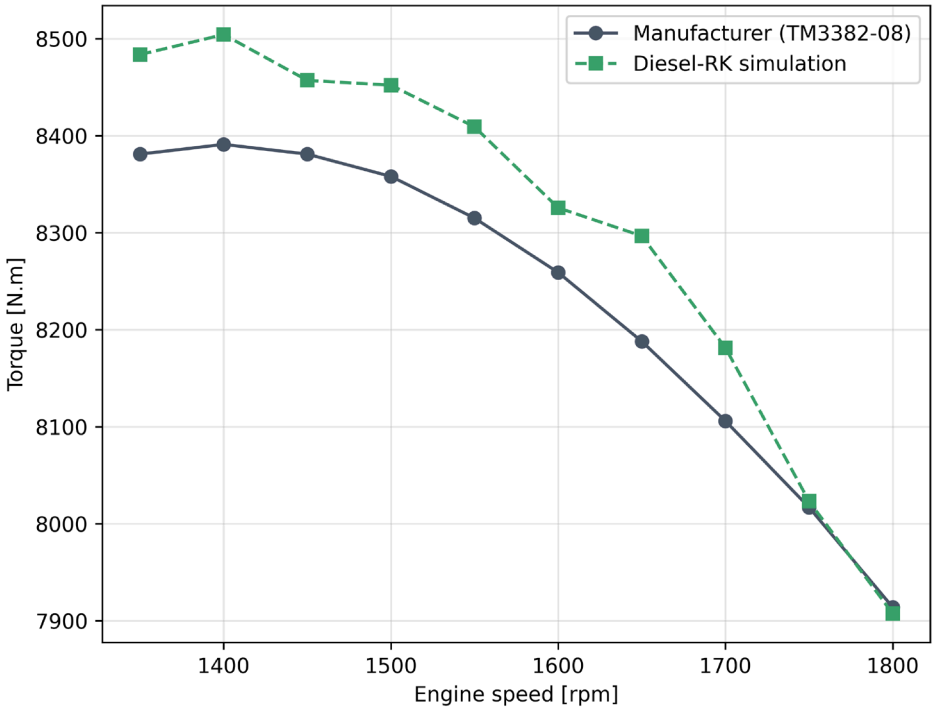

Figure 5. Brake torque as a function of engine speed: Diesel-RK predictions versus manufacturer data.

Figure 6 further shows that BSFC agreement is not uniform across the investigated engine-speed range, with the largest discrepancies occurring at the low- and high-speed regions. The manufacturer-reported experimental BSFC decreases overall from 220.5 g/kWh at 1350 rpm to 204.0 g/kWh at 1800 rpm, although it slightly increases between 1500 and 1600 rpm. In contrast, the Diesel-RK predictions remain comparatively flat at approximately 205.0–207.5 g/kWh between 1350 and 1750 rpm before increasing to approximately 210.3 g/kWh at 1800 rpm. Consequently, Diesel-RK underpredicts BSFC by approximately 5.90% at 1350 rpm and overpredicts it by approximately 3.09% at 1800 rpm. This pattern may reflect limitations in the speed-dependent calibration of the fuel-injection

schedule, turbocharger matching, mechanical-loss, and heat-transfer sub-models, which may not fully reproduce the variation in manufacturer-reported brake efficiency across the full operating-speed range. However, the available manufacturer data cannot isolate the contribution of each factor.

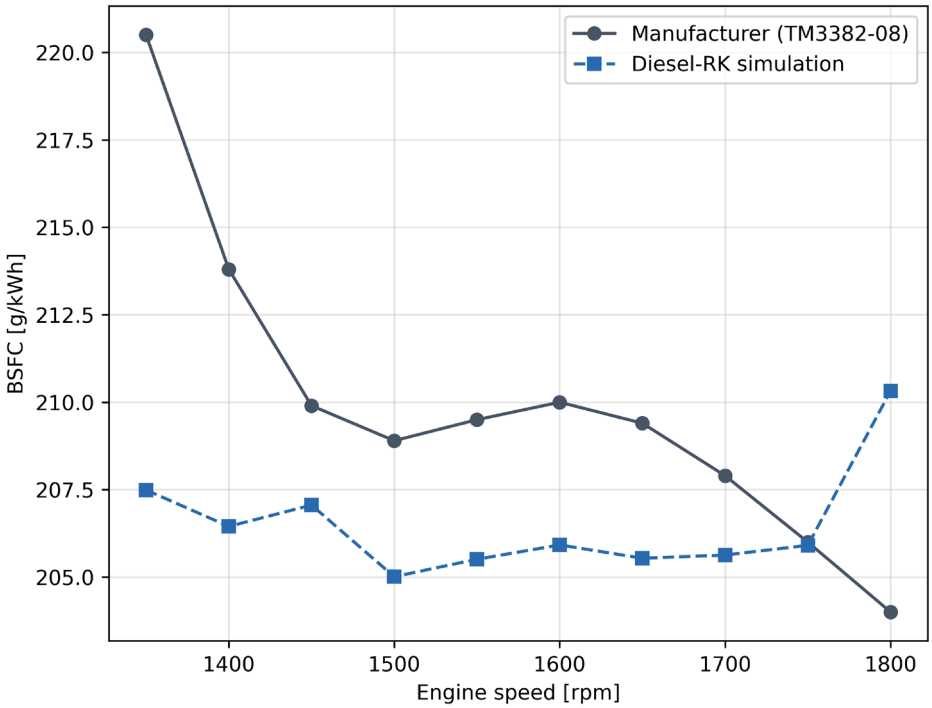

Figure 6. Brake-specific fuel consumption as a function of engine speed: Diesel-RK predictions versus manufacturer data.

After validation, the model was evaluated under representative Arctic operating conditions at Raglan Mine (T = 263 K, p = 0.943 bar), while maintaining the calibrated engine and turbocharger parameters obtained under the reference operating conditions. The baseline engine calibration corresponds to a turbocharger efficiency of η_{TC} = 0.76, a compressor pressure ratio of PR_C = 3.7, a fuel mass per cycle of m_f = 0.3628 g/cycle, and a start of injection SOI = 16° BTDC.

The resulting Arctic operating point, summarized in Table 3, serves as the reference baseline for all subsequent surrogate construction, optimization, and performance comparisons presented in this study.

Table 3. Diesel-RK Arctic baseline for the CAT 3516 diesel generator under representative Raglan Mine operating conditions.

Parameter	Value
P_{eng} (kW)	1532.7
BSFC (g/kWh)	204.51
NO_x (g/kWh)	6.1528
p_{max} (bar)	154.36
η_{TC} (-)	0.76
SOI (°BTDC)	16
PR_C	3.7
m_f (g/cycle)	0.3628

3.2. Design of Experiments

The design space explored in this study was defined by three engine calibration variables: start of injection (SOI ∈ [6°, 20°] BTDC), compressor pressure ratio (PRc ∈ [1.5, 4.0]), and fuel mass per cycle (m_f ∈ [0.25, 0.385] g/cycle). Rather than selecting these bounds arbitrarily, we established them through a series of preliminary high-fidelity Diesel-RK simulations to ensure the optimization domain remained physically meaningful while covering the full range of practically relevant operating conditions.

We first investigated the compressor pressure ratio and start-of-injection limits through a two-dimensional parametric study over PR_C ∈ [1.5, 4.0] and SOI ∈ [0°, 22°] BTDC. As shown in Figure 7, combustion behavior was governed primarily by the compressor pressure ratio. At the lower bound (PR_C = 1.5), combustion duration remained abnormally long (171–182° crank angle) across the entire injection-timing range, whereas increasing the pressure ratio to approximately PR_C = 3.625 reduced combustion duration to values representative of stable diesel combustion (56–65° crank angle). These results indicate that the lower pressure-ratio bound corresponds to the practical limit of acceptable combustion behavior.

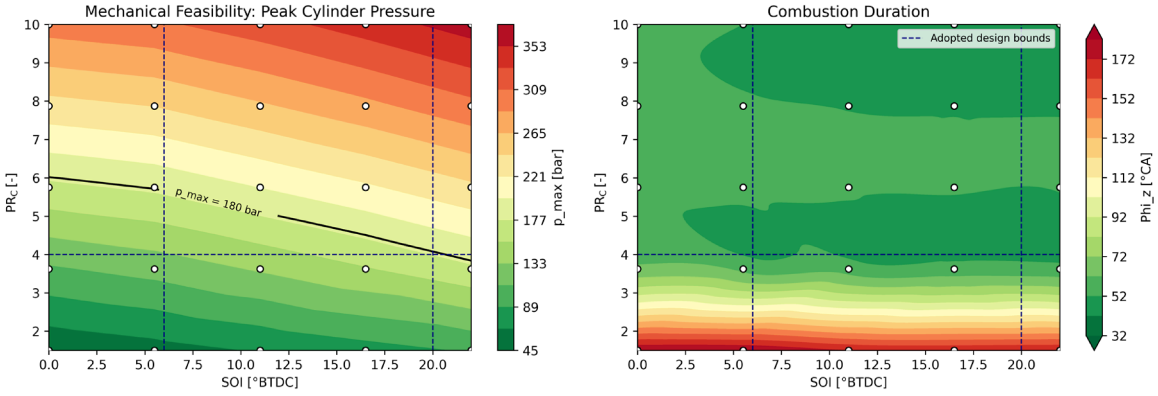

Figure 7. Feasible maps for PR_C and SOI bounds (peak cylinder pressure and combustion duration).

The upper pressure-ratio limit was determined by the mechanical constraint on maximum cylinder pressure. While peak cylinder pressure remained below the adopted limit of 180 bar at PR_C = 3.625, it exceeded this threshold at PR_C = 5.75, where engine performance also deteriorated significantly, with brake power decreasing to only 22–31% of the rated value. Consequently, the selected upper bound of PR_C = 4.0 provides a suitable compromise between extending the exploration domain and maintaining mechanically feasible operating conditions.

A second parametric study refined the lower limit of the start of injection. At SOI = 0° BTDC, the Diesel-RK combustion solver reported an invalid in-cylinder air-fuel composition, accompanied by an excessively long combustion duration (189° crank angle). Stable simulations were first obtained at approximately SOI = 6.67° BTDC, confirming that the adopted lower bound of 6° BTDC remains safely within the physically feasible operating domain. The upper injection-timing limit was independently confirmed during the Sobol sampling campaign, where the only two mechanically infeasible operating points corresponded to SOI ≈ 19.1° BTDC and exceeded the prescribed 180-bar cylinder-pressure limit.

The fuel-mass range was derived from the manufacturer-rated operating condition. The nominal fuel delivery of the CAT 3516 engine, back-calculated from the manufacturer's specification (362.8 L h^{-1} at 1800 rpm), corresponds to approximately 0.353 g/cycle. The upper bound (0.385 g/cycle) was selected to permit limited exploration beyond the rated operating condition, whereas the lower bound (0.25 g/cycle) was verified through high-

fidelity simulation at the most demanding operating condition (SOI = 20° BTDC, PRC = 4.0), yielding physically consistent engine performance while remaining below the maximum cylinder-pressure constraint (P_{eng} = 925.9 kW, p_{max} = 172.2 bar, within the mechanical limit). Based on these results, the preliminary feasibility studies provide the physical basis for the final design space adopted in the optimization: SOI = 6–20° BTDC, PR_C = 1.5–4.0, and m_f = 0.25–0.385 g/cycle. The selected bounds therefore combine manufacturer-rated operating information with Diesel-RK-based combustion stability, engine performance, and mechanical feasibility considerations.

The final training database consisted of a 128-point Sobol low-discrepancy design, followed by a 27-point targeted Latin Hypercube Sampling (LHS) enrichment, yielding 155 high-fidelity Diesel-RK simulations. We introduced the enrichment stage after evaluating candidate calibration points with the largest discrepancies between surrogate predictions and high-fidelity simulations (Section 2.3.1), improving surrogate accuracy in the most critical regions of the design space rather than uniformly increasing sample density.

Of the 155 operating points, 153 satisfied the prescribed mechanical constraint, while the remaining two exceeded the 180-bar cylinder-pressure limit. We intentionally retained these two infeasible points in the training database and explicitly identified them as constraint-violating samples rather than discarding them. This approach lets the Gaussian Process surrogate learn the full physical response of the engine while enforcing mechanical feasibility only during optimization.

Figure 8 illustrates the distribution of the initial 128-point Sobol design across the three pairwise projections of the design space. Figure 9 shows the final enriched database, where the additional Latin Hypercube samples are concentrated in regions identified through high-fidelity validation as exhibiting the largest surrogate prediction errors.

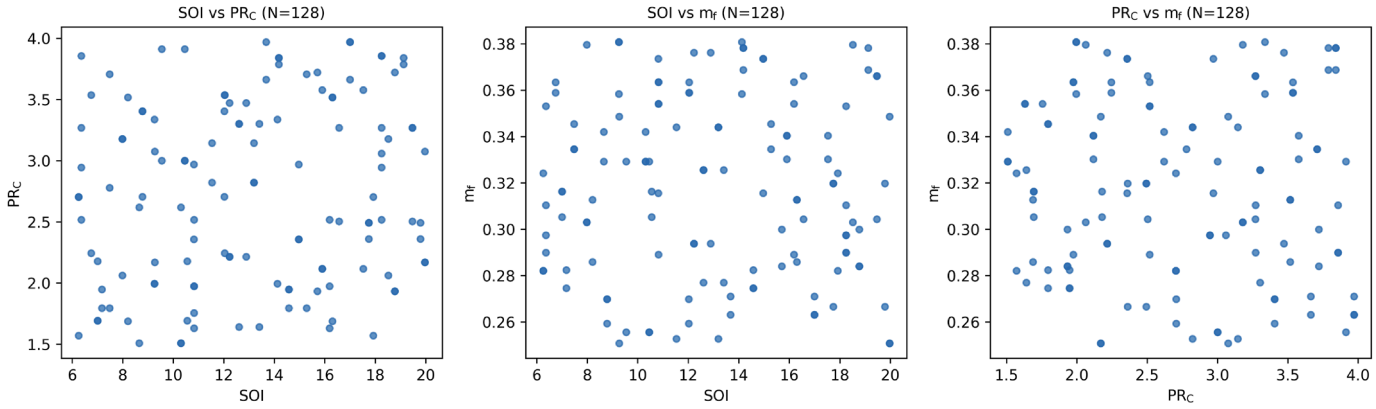

Figure 8. Sobol design of experiments (N = 128), 2D projections.

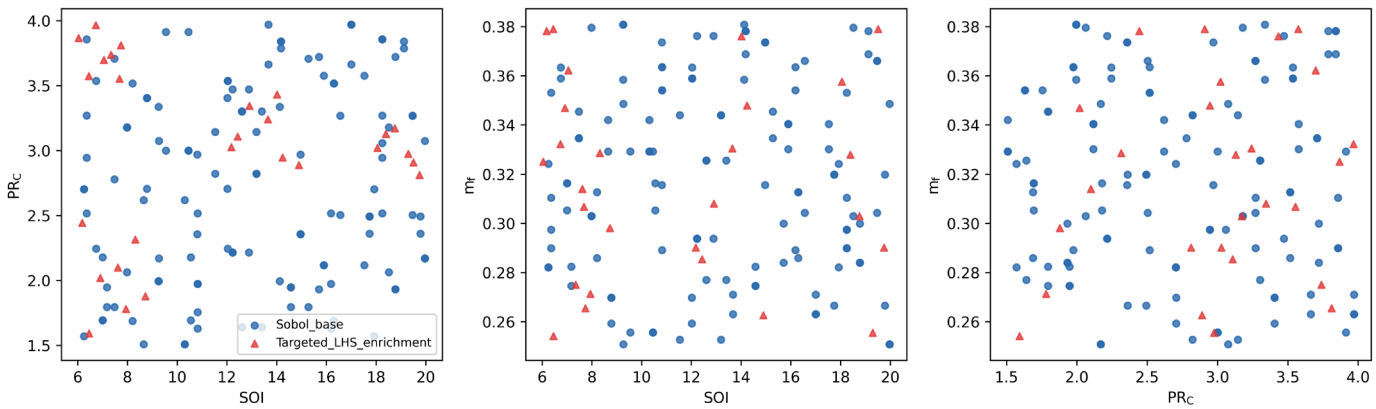

Figure 9. Enrichment design of experiments (N = 155), Sobol base + Targeted LHS enrichment.

3.3. Design of Experiments Sample-Size Convergence

We evaluated convergence of the adaptive design of experiments (DoE) by monitoring both the uniformity of the sampling distribution and the predictive performance of the Gaussian Process surrogate models across successive sampling stages. Table 4 summarizes the Centered Discrepancy (CD) together with the coefficient of determination (R^2) for the four surrogate models after each cumulative sampling stage, corresponding to the initial Sobol designs (32, 96, and 128 samples) and the final enriched database (155 samples, including 153 mechanically feasible operating points).

Table 4. DoE convergence: Centered Discrepancy and surrogate R^2 (N = 32–155).

N	CD	R^2 (P_{eng})	R^2 (BSFC)	R^2 (NOx)	R^2 (p_{max})
32	0.0399	0.9973	0.9506	0.9539	0.9938
96	0.0166	0.9985	0.9828	0.9657	0.9948
128	0.0113	0.9989	0.9876	0.9668	0.9952
155	0.0023	0.9994	0.9942	0.8196	0.9967

As expected, the Centered Discrepancy decreases monotonically with increasing sample size, indicating progressively more uniform coverage of the three-dimensional design space. Simultaneously, the predictive accuracy of all surrogate models improves substantially between 32 and 96 samples and continues to increase, although more gradually, between 96 and 128 samples. This behavior indicates that the initial Sobol sampling efficiently captures the engine's global response and approaches convergence after approximately 128 simulations.

The subsequent 27-point targeted Latin Hypercube enrichment was not intended to improve global sampling uniformity but rather to refine surrogate accuracy in localized regions identified through high-fidelity validation as exhibiting the largest prediction errors (Section 2.3.1). Consequently, the additional samples were deliberately concentrated within highly nonlinear regions of the design space rather than distributed uniformly.

This enrichment strategy has little influence on the already excellent predictive performance of the brake power, BSFC, and peak cylinder pressure surrogates, whose R^2 values continue to improve. In contrast, the apparent reduction in the NO_x surrogate coefficient of determination from 0.9668 (128 samples) to 0.8196 (155 samples) does not indicate a deterioration of the surrogate model. Instead, it reflects the deliberate inclusion of additional high-error operating conditions that make the independent validation dataset substantially more challenging. The decrease in R^2 therefore results from a more demanding validation problem rather than reduced surrogate capability.

Overall, these results demonstrate that surrogate performance depends not only on the number of training samples but also on their distribution within the design space. The adaptive Sobol–Latin Hypercube strategy successfully combines efficient global exploration with targeted local refinement, producing a compact yet highly informative database for surrogate-assisted optimization.

Figure 10 illustrates the evolution of surrogate accuracy throughout the sampling process, while Table 4 summarizes the corresponding convergence statistics.

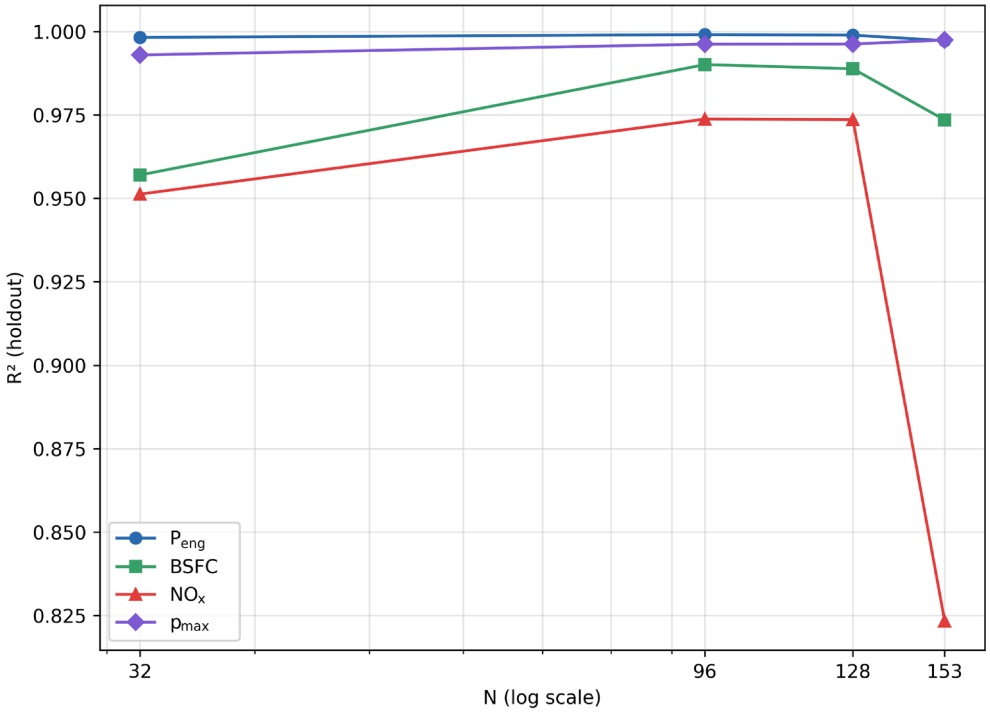

Figure 10. Surrogate R^2 convergence across DoE stages (N = 32 to 153).

3.4. Gaussian Process (GP) Surrogate Performance

Whereas Section 3.1 validates the Diesel-RK model against manufacturer performance data, independent of any surrogate, the verification reported in this section concerns the Gaussian Process surrogate's ability to reproduce Diesel-RK's output, not experimental data.

We evaluated the predictive performance of the four Gaussian Process (GP) surrogate models using the validation methodology described in Section 2.3.3. Table 5 summarizes performance on the final enriched database, while Figure 11 presents the corresponding leave-one-out cross-validation (LOO-CV) parity plots with the associated 95% predictive uncertainty envelopes.

Table 5. GP surrogate performance on the final 155-point dataset (80/20 holdout).

Output	R^2	RMSE	MAE	MAPE (%)	Empirical 95% PI Coverage
P_{eng}	0.9974	8.53 kW	5.64 kW	0.47%	93.55%
BSFC	0.9717	1.67 g/kWh	1.15 g/kWh	0.52%	93.55%
NO_x	0.8196	0.664 g/kWh	0.439 g/kWh	9.71%	93.55%
p_{max}	0.9976	1.42 bar	0.97 bar	0.87%	96.77%

Overall, surrogate models exhibit excellent predictive capability. The surrogates for brake power (P_{eng}), brake-specific fuel consumption (BSFC), and maximum cylinder pressure (p_{max}) all achieve coefficients of determination exceeding 0.97, with mean absolute percentage errors below 1%, showing that the Gaussian Process models accurately reproduce the high-fidelity Diesel-RK simulations across the full calibration domain.

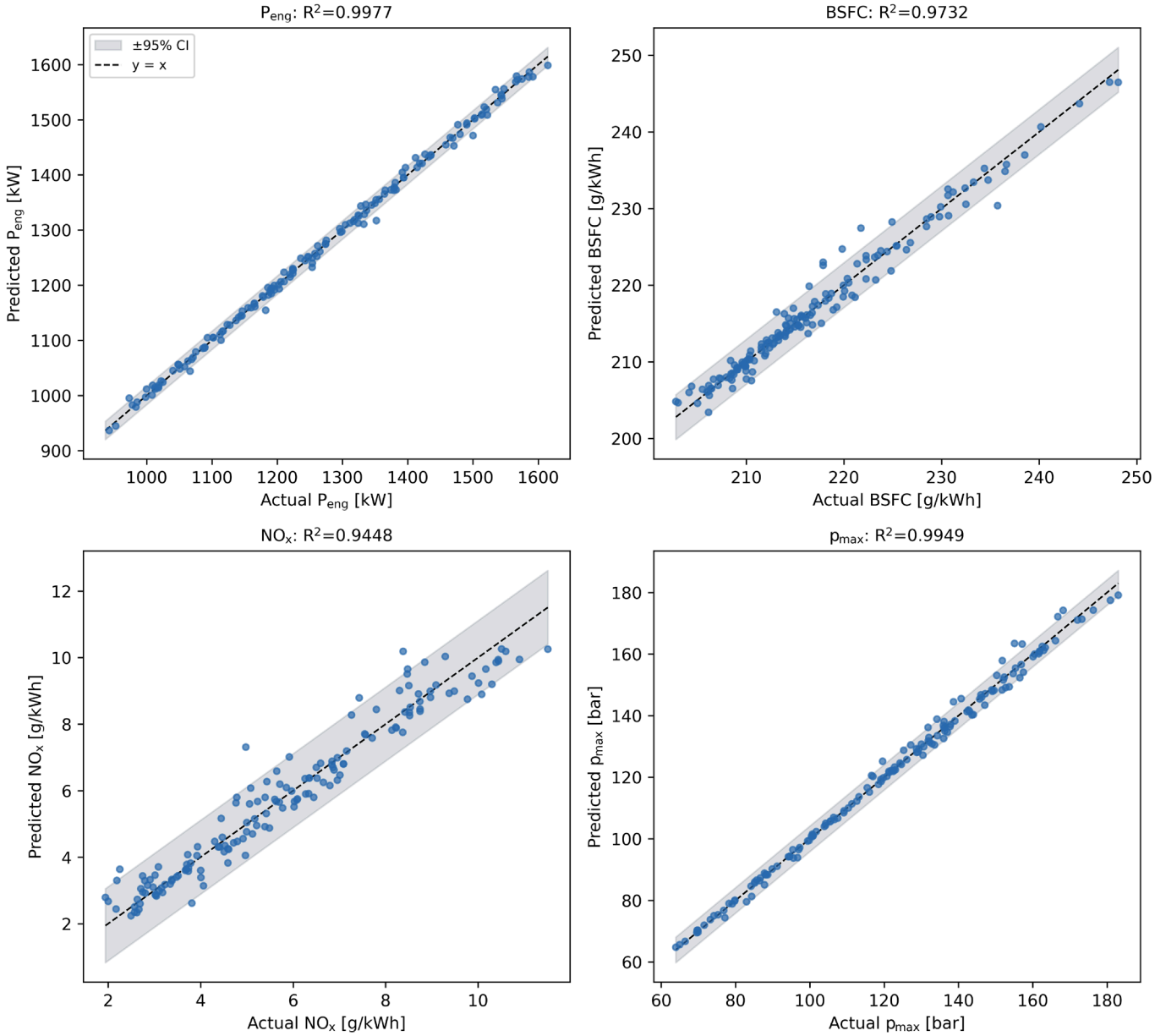

Figure 11. Leave-one-out cross-validation parity plots for the four Gaussian Process surrogate models, including the 95% predictive uncertainty envelope (N = 155).

The NO_x emissions surrogate shows comparatively lower predictive accuracy (R^2 = 0.8196; MAPE = 9.71%), reflecting the substantially greater nonlinearity of NO_x formation than the other response variables. For NO_x specifically, the surrogate error quantified in this section is measured relative to Diesel-RK predictions, not to experimental NO_x measurements. Because experimental NO_x data were unavailable for the present CAT 3516 configuration, interpret the resulting NO_x predictions as model-based engine-out estimates.

As discussed later in Section 3.6, global sensitivity analysis reveals that NO_x emissions are governed by stronger nonlinear interactions among the calibration variables, making this response inherently more challenging to approximate using surrogate models. Moreover, the targeted enrichment strategy intentionally introduced additional training and validation samples within the most complex regions of the design space, thereby creating a substantially more demanding validation dataset. Consequently, the lower coefficient of determination should be interpreted as the result of a more challenging prediction problem rather than an indication of inadequate surrogate performance.

The parity plots shown in Figure 11 further confirm the quality of the surrogate models. For all four response variables, the predictions closely follow the identity line. At the same time, the shaded 95% confidence envelopes and point-specific uncertainty bars demonstrate that the Gaussian Process models provide not only accurate point predictions but also statistically meaningful estimates of predictive uncertainty. This uncertainty quantification constitutes a key advantage of the proposed framework, as it supports the confidence-based validation and decision-making procedures developed in the subsequent optimization stages.

Empirical GP prediction-interval coverage was computed as the proportion of the 31-point post-enrichment holdout observations (80/20 split, random_state = 42) falling within the predicted $\mu \pm 1.96\sigma$ interval, for each output. Because the holdout partition was generated after adaptive enrichment, these results quantify internal post-enrichment coverage conditional on the enriched sampling distribution and are not interpreted as an independent end-to-end uncertainty calibration.

The lower accuracy of the NO_x surrogate is consistent with the strongly nonlinear nature of NO_x formation, as represented in Diesel-RK by the extended Zeldovich mechanism, which is highly sensitive to the thermal history of combustion and to changes in SOI. This response complexity, combined with the more demanding validation dataset created by targeted enrichment, makes NO_x harder to approximate than brake power, BSFC, and p_{max}. Accordingly, NO_x point predictions are interpreted with greater caution, and the selected operating point is confirmed by high-fidelity Diesel-RK simulation.

3.5. Response Surfaces and Predictive Uncertainty

To visualize the surrogate models and the relationships between the engine calibration variables and the performance objectives, we generated two-dimensional and three-dimensional response surfaces from the Gaussian Process (GP) surrogate models developed in Section 3.4. Unlike classical Response Surface Methodology (RSM), these surfaces directly represent the probabilistic GP surrogates and do not rely on polynomial approximations or desirability-based optimization.

Figure 12 presents two-dimensional response surfaces for the four surrogate outputs over the (SOI, PR_C) plane, evaluated at the Arctic baseline fuel mass of $m_f = 0.3628$ g/cycle. The color maps show the surrogate mean predictions, while the superimposed contours show the Gaussian Process predictive standard deviation, illustrating both the predicted engine response and the associated model confidence. Figure 13 shows the corresponding three-dimensional representations.

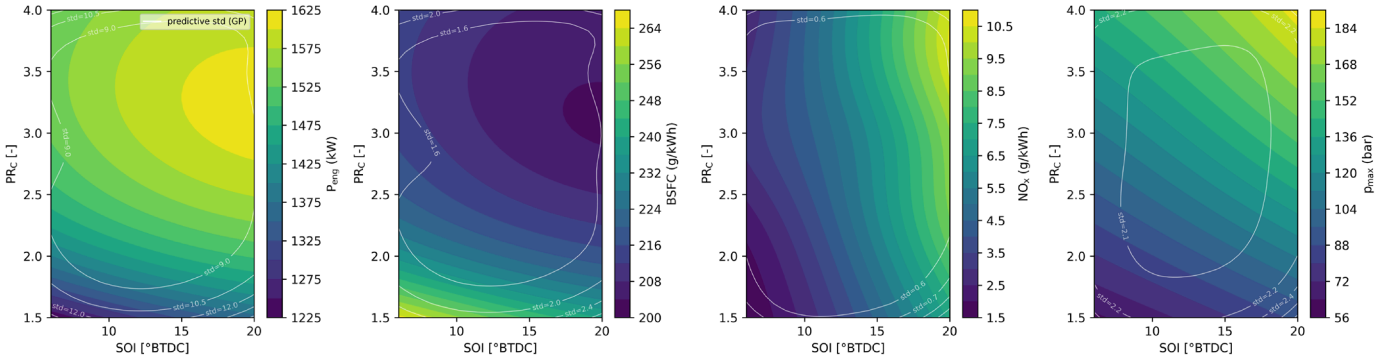

Figure 12. Two-dimensional Gaussian Process response surfaces with predictive uncertainty contours.

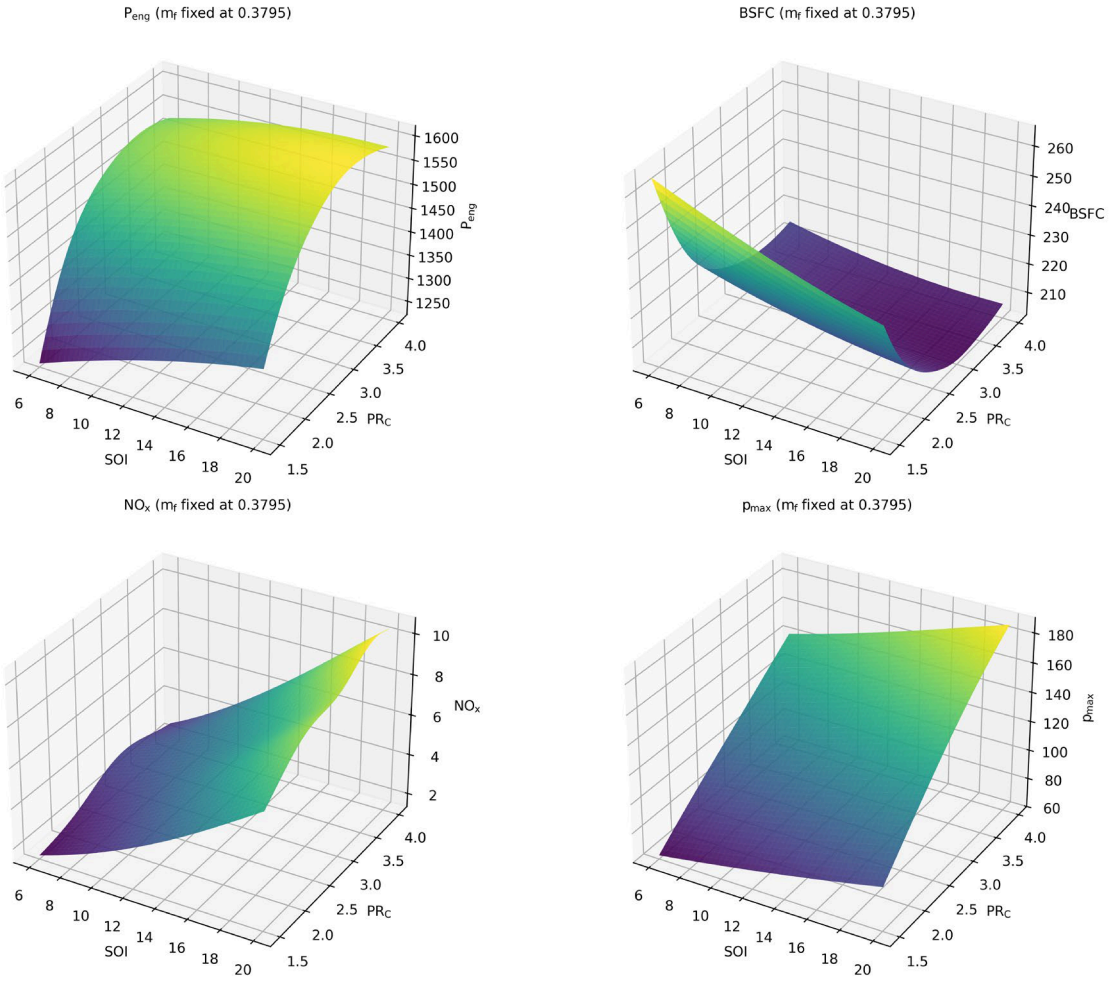

Figure 13. Three-dimensional Gaussian Process response surfaces.

The response surfaces clearly illustrate the principal trends governing engine performance. Brake power increases with both start of injection and compressor pressure ratio, whereas brake-specific fuel consumption shows approximately inverse behavior, reflecting improved combustion efficiency at higher intake-air pressure and more advanced injection timing. In contrast, NO_x emissions display the strongest nonlinear behavior among the four response variables, increasing rapidly with advancing injection timing and elevated compressor pressure ratios. This behavior is consistent with the higher combustion temperatures associated with these operating conditions and explains the greater modeling complexity observed for the NO_x surrogate in Section 3.4.

The predictive uncertainty is not uniformly distributed throughout the design space. While the Gaussian Process models show high confidence across most of the operating domain, larger predictive standard deviations occur in localized regions with stronger nonlinear engine behavior, particularly in portions of the domain associated with low NO_x emissions. These uncertainty maps provide valuable information for interpreting the optimization results and identifying regions where high-fidelity Diesel-RK verification is most beneficial.

3.6. Sobol Global Sensitivity Analysis

We performed variance-based global sensitivity analysis on the Gaussian Process surrogate models using the 128-point Sobol base dataset, before the targeted enrichment stage (Section 2.3.1). This choice ensures that the sensitivity indices characterize the engine's

intrinsic response over the uniformly sampled design space, without being influenced by the localized sampling introduced to improve surrogate accuracy during optimization.

Table 6 summarizes the dominant design variable together with its first-order (S_1) and total-order (S_T) Sobol sensitivity indices for each of the four surrogate outputs, while Figure 14 provides a graphical comparison of the sensitivity contributions.

Table 6. Dominant design variable and Sobol sensitivity indices for the four surrogate outputs.

Output	Dominant	S_1	S_T
P_{eng}	m_f	0.917	0.941
BSFC	PR_C	0.593	0.840
NO_x	SOI	0.887	0.892
p_{max}	PR_C	0.829	0.833

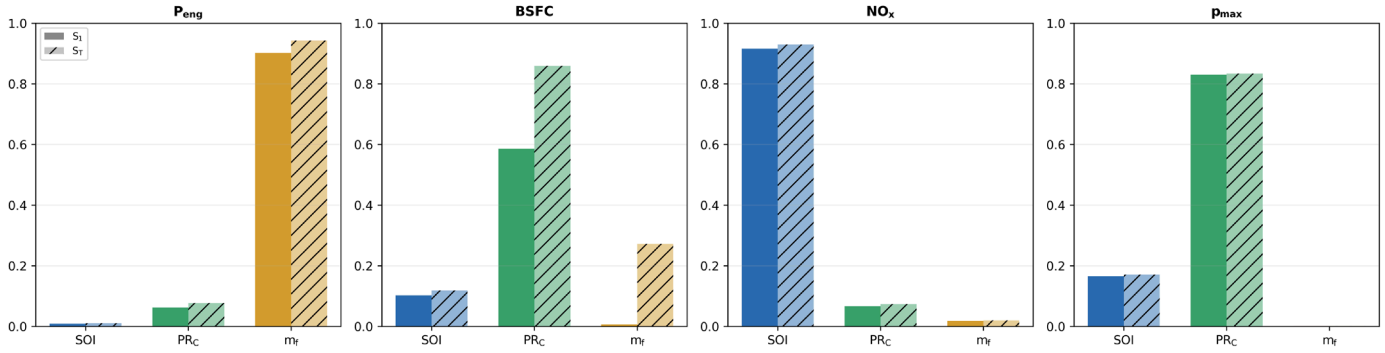

Figure 14. First-order and total-order Sobol sensitivity indices for the four surrogate outputs.

The analysis reveals that each response variable is primarily controlled by a single calibration parameter. Brake power is dominated by the fuel mass per cycle (m_f, S_1 = 0.917), reflecting the direct influence of fuel input on engine power output. Both brake-specific fuel consumption (BSFC) and maximum cylinder pressure (p_{max}) are governed predominantly by the compressor pressure ratio (S_1 = 0.593 and 0.829, respectively), highlighting the importance of intake-air pressurization in determining combustion efficiency and peak in-cylinder loading. In contrast, NO_x emissions are controlled primarily by the start of injection (SOI) (S_1 = 0.887), consistent with the strong influence of injection timing on combustion phasing and flame temperature.

Comparison of the first-order and total-order Sobol indices provides additional insight into interaction effects among the calibration variables. For NO_x emissions and maximum cylinder pressure, the close agreement between S_1 and S_T indicates that the responses are governed predominantly by the corresponding main effects, with relatively weak interactions among variables. Conversely, the noticeably larger difference between the first-order and total-order indices for BSFC suggests that fuel efficiency depends not only on the compressor pressure ratio but also on its interaction with the fuel mass per cycle and the start of injection. This result explains the more complex BSFC response surface and underscores the importance of optimizing the three calibration variables simultaneously.

Overall, the global sensitivity analysis confirms that the surrogate models capture physically meaningful relationships consistent with diesel combustion theory, thereby providing additional confidence in their use for surrogate-assisted optimization and supporting the engineering interpretation of the optimal calibration strategy discussed in Section 4.2.

3.7. Multi-Objective Optimization

The four optimization algorithms described in Section 2.4.2, NSGA-II, classical Genetic Algorithm (GA), Grey Wolf Optimizer (GWO), and Bayesian Optimization using Gaussian Processes (BO-GP), were applied to the enriched 155-point Gaussian Process surrogate model. Each algorithm received a computational budget appropriate to its search strategy (Table 2), enabling a representative comparison of fundamentally different optimization paradigms.

We evaluated optimization performance using the three-dimensional hypervolume indicator, which measures both convergence toward the Pareto front and the diversity of the obtained non-dominated solutions. As summarized in Table 7, NSGA-II achieved the highest hypervolume, indicating the most complete approximation of the Pareto front. GWO and the classical GA produced comparable results, whereas BO-GP achieved a lower hypervolume. This outcome is consistent with its sequential optimization strategy and substantially smaller evaluation budget, which prioritizes efficient local exploration over broad Pareto-front coverage.

Table 7. Hypervolume comparison of the four optimization algorithms.

Algorithm	N (Filtered)	Hypervolume	Rank
NSGA-II	200	392,795	1
GWO	142	387,300	2
GA	20	386,921	3
BO-GP	10	367,307	4

Despite these differences in search strategy and Pareto-front coverage, the four algorithms converged toward remarkably similar optimal objective values (Table 8). The minimum NO_x emissions varied only between 2.721 $\pm$ 0.002 and 2.792 $\pm$ 0.0021 g/kWh, while the minimum BSFC ranged from 203.37 $\pm$ 0.00 to 204.44 $\pm$ 0.71 g/kWh. The largest variation was observed for maximum brake power, which ranged from 1574.0 $\pm$ 16.86 to 1606.4 $\pm$ 0.07 kW. This strong agreement among optimization algorithms adds confidence that the identified Pareto front reflects the underlying engine-response characteristics rather than artifacts of a particular optimization technique.

Table 8. Best objective values obtained by each optimization algorithm.

Algorithm	Non-Dominated Solutions	Max P_{eng} (kW)	Min BSFC (g/kWh)	Min NO_x (g/kWh)
NSGA- II	200	1606.4 $\pm$ 0.07	203.37 $\pm$ 0.00	2.721 $\pm$ 0.002
GA	20	1606.0 $\pm$ 0.22	203.41 $\pm$ 0.05	2.757 $\pm$ 0.009
GWO	142	1601.7 $\pm$ 1.13	203.75 $\pm$ 0.17	2.772 $\pm$ 0.0014
BO-GP	10	1574.0 $\pm$ 16.86	204.44 $\pm$ 0.71	2.792 $\pm$ 0.0021

We combined the non-dominated solutions from the reproducible optimization runs of the four algorithms to form a unified Pareto front comprising 284 solutions. We ran each algorithm once using the fixed random seed specified in Table 2, consistent with comparing optimization paradigms rather than statistically benchmarking stochastic algorithms. The resulting front spans 1483.5–1606.4 kW for brake power, 203.37–219.79 g/kWh for BSFC, and 2.720–8.849 g/kWh for NO_x emissions. Although brake power and BSFC vary by approximately8% across the Pareto front, NO_x emissions vary by more than threefold, showing that pollutant emissions drive the main trade-off in the engine calibration problem.

This observation confirms the need to adopt a multi-objective optimization framework rather than optimizing fuel consumption or engine performance alone.

Figure 15 presents the combined Pareto front, with each solution accompanied by its corresponding 95% Gaussian Process predictive uncertainty. These uncertainty estimates add confidence to the optimization results by explicitly identifying the surrogate-model certainty associated with each Pareto-optimal operating point.

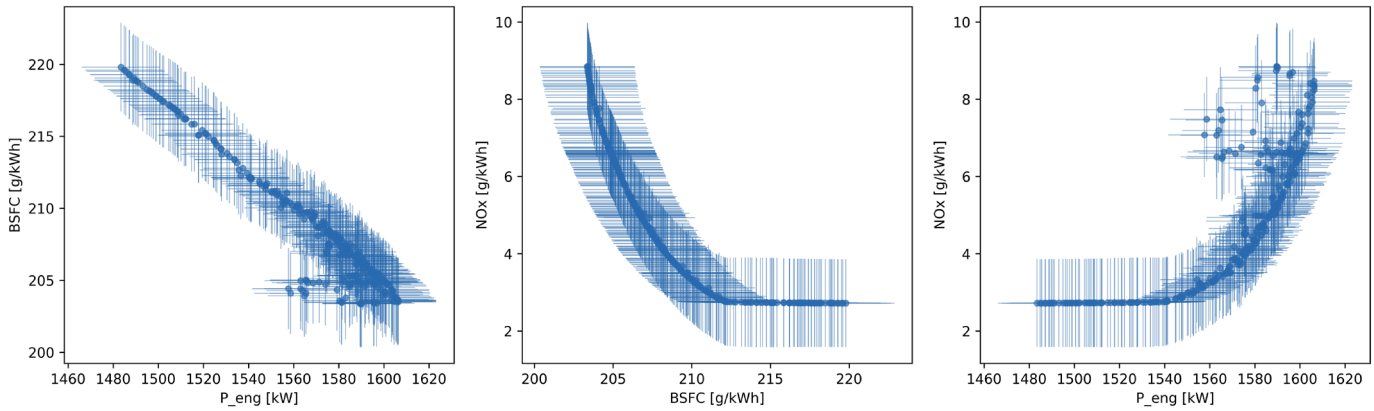

Figure 15. Combined Pareto front showing the non-dominated solutions obtained by the four optimization algorithms together with their corresponding 95% Gaussian Process predictive uncertainty.

3.8. Multicriteria Decision-Making

The SIMUS multicriteria decision-making method was applied to the combined 284-point Pareto front obtained in Section 3.7 to identify the most appropriate operating point for practical engine calibration. We evaluated eleven representative alternatives, uniformly distributed across the Pareto front, using the two independent SIMUS ranking procedures described in Section 2.5.1. Appendix D.1 provides the complete ranking results.

Both the Efficient Results Matrix (ERM) and the Project Dominance Matrix (PDM) independently identified Alternative A4 (hereafter K) as the highest-ranked solution. The agreement between these two independent ranking procedures confirms the robustness and reproducibility of the selected operating point while avoiding the subjectivity associated with weighting-factor-based multicriteria decision-making methods.

The selected operating point corresponds to the Pareto knee-point solution selected by the SIMUS procedure:

- SOI = 12.706° BTDC;
- PR_C = 3.430;
- m_f = 0.3795 g/cycle.

Alternative A6 ranked second, and A7 ranked third under both SIMUS procedures. The remaining alternatives received identical scores because each represented an extreme solution that optimized only one objective while being dominated on the other two objectives. Consequently, no meaningful ranking can be established among these remaining Pareto-optimal solutions [49].

The consistent identification of Alternative K by both SIMUS procedures demonstrates that the selected operating point represents a balanced compromise among brake power, fuel consumption, and NO_x emissions, providing a robust basis for the subsequent high-fidelity Diesel-RK validation.

As a robustness check against the SIMUS ranking, TOPSIS was applied to the same 11 representative alternatives presented in Appendix D.2, considering P_{eng} as a benefit criterion and BSFC and NO_x as cost criteria. With vector normalization and equal weights of one-third for each criterion, the complete ranking was A9 > A10 > A8 > A11 > A7 > A6

> K > A3 > A2 > A5 > A1. Thus, K ranked seventh, with a closeness coefficient of 0.5622. The four alternatives with the lowest NO_x values: A9, A10, A8, and A11 occupied the first four positions. This result is explained by the considerably greater variation in NO_x, which spans approximately a factor of 3.03 across the alternatives, from 2.720 to 8.249 g/kWh. In comparison, P_{eng} and BSFC vary by only 8.28% and 7.95%, respectively. Consequently, NO_x has a much stronger influence on the vector-normalized TOPSIS distances. With benefit-oriented min–max normalization and the same equal weights, TOPSIS ranked A6 first (0.7413), K second (0.7255), and A7 third (0.7205). These are the same three leading alternatives identified by SIMUS, although A6 and K exchange positions. These results reinforce SIMUS as the primary multicriteria decision-making tool in the proposed framework, as it provides a robust, reproducible selection of the preferred operating point while avoiding the sensitivity to normalization procedures observed with TOPSIS. Appendix D.2 reports the TOPSIS results.

Sensitivity analysis indicates that K remains top-ranked for NO_x RHS within −2.1% to +14.6% of its mean value; beyond this range, the ranking shifts to A6 or A3. -Point K ranks first only between 0% and +10%. Below −2.1%, A6 leads. At +15%, A3 overtakes. Third and fourth positions also shift: A6 drops from second to fourth as the perturbation moves from negative to positive, despite leading on the negative side (Appendix D.3).

3.9. High-Fidelity Validation

The operating point K, selected through the SIMUS multicriteria decision-making procedure (Section 3.8), was independently re-evaluated using the high-fidelity Diesel-RK model under the same Arctic operating conditions employed throughout this study, following the validation procedure described in Section 2.5.2. Table 9 compares the Gaussian Process (GP) surrogate predictions with the corresponding high-fidelity Diesel-RK simulation results.

Table 9. Comparison between Gaussian Process predictions and high-fidelity Diesel-RK simulations at operating point K.

Output	GP Prediction	Diesel-RK	Relative Error	Deviation	Within 95%?
P_{eng} (kW)	1588.575 ± 8.727	1589.4	−0.05%	0.09σ	Yes
BSFC (g/kWh)	206.481 ± 1.524	206.290	+0.09%	−0.13σ	Yes
NO_x (g/kWh)	5.156 ± 0.780	4.499	+14.6%	−0.84σ	Yes

The surrogate predictions agree well with the high-fidelity Diesel-RK simulations. Although the relative error for NO_x is larger than for brake power and BSFC, the prediction remains well within the surrogate's 95% predictive interval, corresponding to a standardized deviation of only −0.84σ. Likewise, the brake power and BSFC predictions differ from the high-fidelity results by only 0.09σ and −0.13σ, respectively. These results demonstrate that the Gaussian Process models accurately quantify not only the expected response but also the associated predictive uncertainty.

Compared with the Arctic baseline operating condition (P_{eng} = 1532.7 kW, BSFC = 204.51 g/kWh, NO_x = 6.1528 g/kWh), the validated operating point K increases brake power by 3.7%, increases brake-specific fuel consumption by only 0.87%, and reduces engine-out NO_x emissions by 26.9%. These results illustrate the principal trade-off identified by the multi-objective optimization framework: a substantial reduction in pollutant emissions can be achieved with only a marginal increase in fuel consumption while simultaneously improving engine power output.

The 14.6% discrepancy observed at point K indicates that the NO_x surrogate has lower local predictive reliability than the power and BSFC surrogates. The final NO_x performance at K was established through an independent Diesel-RK re-evaluation (4.499 g/kWh), and this high-fidelity value was used to calculate the reported 26.9% NO_x reduction. However, it may affect the ordering of closely competing surrogate-generated Pareto solutions. Therefore, shortlisted alternatives with comparable NO_x predictions should be evaluated directly using Diesel-RK before final engineering selection.

The practical significance of this result lies in the favorable trade-off: a 26.9% reduction in engine-out NO_x is achieved alongside a 3.7% increase in brake power, while the associated BSFC deterioration is limited to 0.87%. Thus, the NO_x reduction is not achieved through power derating, and the additional power capability comes with only a limited fuel-efficiency penalty. For a stationary diesel generator, this combination is operationally attractive because it improves available engine output and emissions performance while largely preserving fuel-specific efficiency.

The validated operating point is highlighted on the combined Pareto front in Figure 16, confirming that the surrogate-assisted optimization solution is consistent with the high-fidelity thermodynamic model and represents a robust compromise among the three optimization objectives.

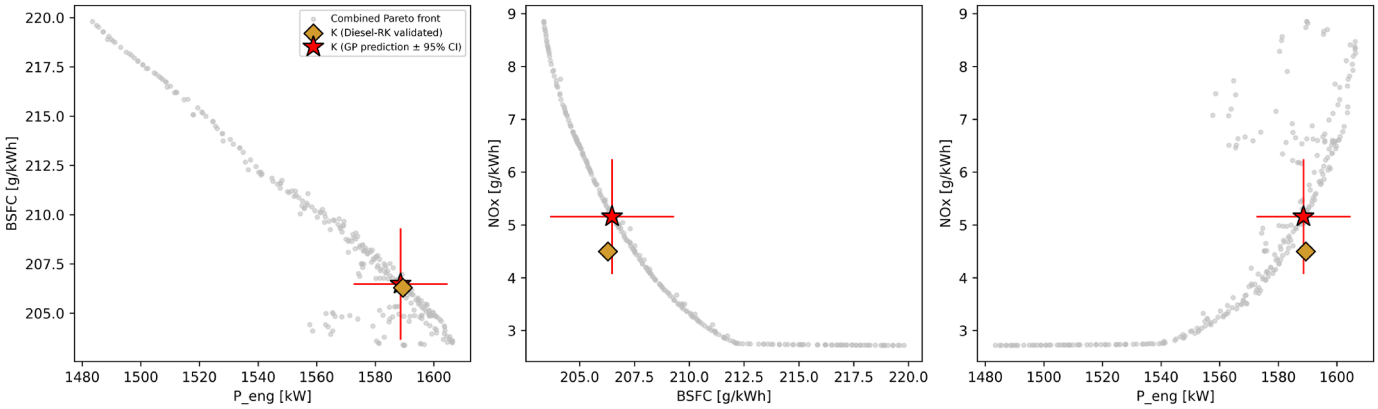

Figure 16. Combined Pareto front highlighting the SIMUS-selected operating point K, validated using the high-fidelity Diesel-RK model.

The limitation discussed in Section 2.3.3 concerns the independence of the dataset used to assess global surrogate performance and uncertainty coverage. It does not affect the pointwise high-fidelity verification of the selected knee point K. After selection, we independently recomputed the predicted responses at K using Diesel-RK, and we did not include K in the enriched training or holdout datasets. This comparison therefore provides an independent, high-fidelity verification of the predicted performance at K, but it is not used to establish global uncertainty calibration.

3.10. Cross-Validation Using the Native Diesel-RK Optimizer

To independently assess the proposed surrogate-assisted optimization framework, we applied the native Diesel-RK optimizer directly to the high-fidelity thermodynamic model, following the procedure described in Section 2.5.3. Unlike the proposed framework, which simultaneously optimizes three competing objectives, the Diesel-RK optimizer performs single-objective optimization using the Rosenbrock direct-search method. We treated the start of injection (SOI) and compressor pressure ratio (PR_C) as decision variables, while fixing the fuel mass per cycle (m_f) at its Arctic baseline value.

We investigated three objective functions available within Diesel-RK independently: minimizing brake-specific fuel consumption (BSFC), maximizing brake mean effective

pressure (BMEP), and minimizing the composite emission index (SE). Table 10 compares the resulting operating points with the Arctic baseline.

Table 10. Operating points obtained using the Diesel-RK native single-objective optimizer.

Point	SOI (°)	PR_C	P_{eng} (kW)	ΔP_{eng}	BSFC (g/kWh)	ΔBSFC	NO_x (g/kWh)	ΔNO_x
Baseline	16.000	3.700	1532.7	-	204.51	-	6.1528	-
BSFC-optimal	20.000	3.400	1543.3	+0.69%	203.11	−0.68%	8.4913	+38.0%
BMEP-optimal	18.789	3.475	1542.8	+0.66%	203.17	−0.66%	7.7090	+25.3%
SE-optimal	6.134	3.883	1424.1	−7.09%	220.11	+7.63%	2.1793	−64.6%

The two performance-oriented objective functions (BSFC minimization and BMEP maximization) converged toward similar regions of the design space, characterized by relatively advanced injection timing and moderate compressor pressure ratios. Both operating points produced only modest improvements in brake power and fuel consumption (less than 1% relative to the baseline) but at the cost of a substantial increase in NO_x emissions (25–38%). This behavior is expected because neither objective function explicitly accounts for pollutant emissions, allowing the optimizer to improve efficiency by advancing combustion phasing.

Conversely, minimizing the composite emission index (SE) led to a markedly different operating point characterized by delayed combustion phasing and a higher compressor pressure ratio. This solution reduced NO_x emissions by 64.6%, but only at the expense of a 7.1% reduction in brake power and a 7.6% increase in fuel consumption. The SE optimization therefore represents the opposite extreme of the engine performance-emissions trade-off.

None of the three single-objective operating points approaches the balanced performance achieved by the SIMUS-selected operating point K (Section 3.9), which simultaneously delivers a 3.7% increase in brake power, only a 0.87% increase in BSFC, and a 26.9% reduction in NO_x emissions relative to the Arctic baseline. This comparison demonstrates that optimizing a single performance criterion, regardless of the objective selected, cannot reproduce the balanced trade-offs obtained through the proposed tri-objective optimization framework.

Figure 17 compares the three Diesel-RK operating points, the Arctic baseline, and the selected operating point K.

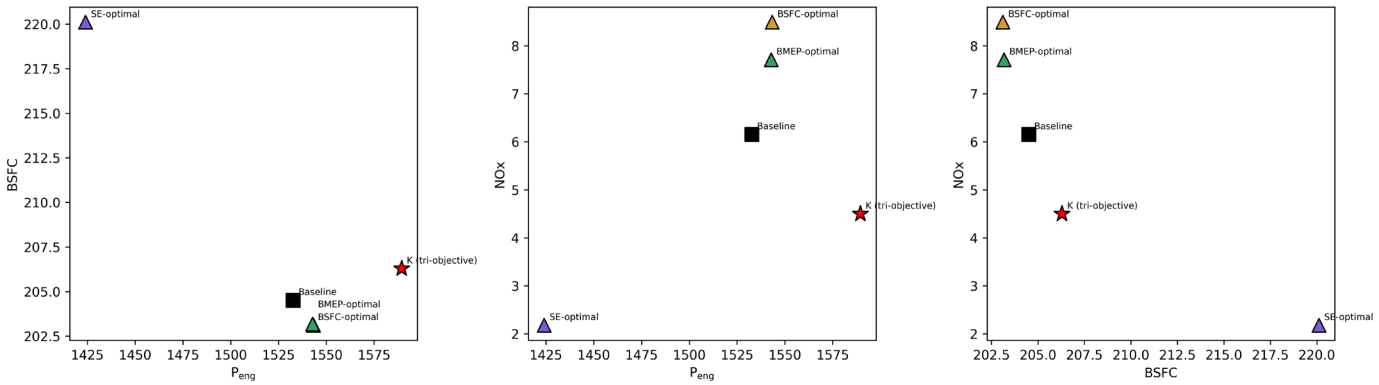

Figure 17. Comparison of the Diesel-RK single-objective operating points, the Arctic baseline, and the SIMUS-selected operating point K.

4. Discussion

4.1. The Role of Predictive Uncertainty in Surrogate-Assisted Optimization

A distinguishing feature of the proposed framework is the systematic use of Gaussian Process (GP) predictive uncertainty throughout the entire calibration workflow rather than relying solely on surrogate mean predictions. Predictive uncertainty is incorporated consistently at every stage of the methodology: during surrogate validation through the parity plots (Figure 11), in the visualization of the response surfaces (Figures 12 and 13), during the interpretation of the combined Pareto front (Figure 15), and finally in the independent high-fidelity validation of the selected operating point K (Figure 16). Consequently, predictive uncertainty becomes an integral component of the optimization and decision-making process rather than a post-processing indicator.

The surrogate models exhibit excellent predictive capability for brake power, brake-specific fuel consumption, and maximum cylinder pressure, with coefficients of determination exceeding 0.97 (Table 5). In contrast, the NO_x surrogate exhibits comparatively lower predictive accuracy (R^2 = 0.82) and greater spatial variability across the design space. The global sensitivity analysis (Table 6) indicates that this behavior is not a limitation of the surrogate model itself but rather reflects the underlying combustion physics. NO_x emissions are governed predominantly by the start of injection (S_1 = 0.887), whose influence on peak combustion temperature through the extended Zeldovich mechanism is strongly nonlinear. By comparison, brake power, BSFC, and maximum cylinder pressure show more distributed sensitivities across the three calibration variables, resulting in smoother response surfaces that Gaussian Process models can approximate more readily.

Validating the selected operating point K demonstrates the value of uncertainty-aware surrogate modeling. Although the GP prediction for NO_x differs from the corresponding Diesel-RK result by 14.6%, representing the largest relative error among the three optimization objectives, the prediction remains well within the surrogate's 95% predictive interval (Table 9). Likewise, the predictions for brake power and BSFC differ from the high-fidelity simulations by less than 0.15 predictive standard deviations. These results demonstrate that the surrogate accurately characterizes not only the expected engine response but also the confidence associated with its predictions. Consequently, the predictive uncertainty, rather than the surrogate mean prediction alone, provides the appropriate basis for evaluating candidate operating points and selecting robust engine calibrations.

4.2. Physical Interpretation of the Optimal Calibration

The selected operating point K (SOI = 12.706°, PR_C = 3.430, m_f = 0.3795 g/cycle) achieves a 26.9% reduction in NO_x emissions relative to the Arctic baseline while simultaneously increasing brake power by 3.7% and incurring only a marginal 0.87% increase in brake-specific fuel consumption. This combination represents a favorable engineering compromise, demonstrating that substantial emission reductions can be achieved without sacrificing engine performance. The reported improvements refer to engine-level calibration under pneumatic assistance and should not be interpreted as net performance gains of the complete wind–CAES–diesel energy system.

The optimized calibration is fully consistent with the sensitivity analysis presented in Section 3.6. The start of injection (SOI), identified as the dominant parameter controlling NO_x formation, is moderately retarded relative to the baseline value (12.706° versus 16° BTDC). This adjustment delays the main heat-release phase, reducing peak combustion temperature and consequently suppressing thermal NO_x formation through the extended Zeldovich mechanism. At the same time, the selected injection timing remains well within the region of stable combustion, avoiding the low-SOI operating conditions where

combustion efficiency deteriorates and surrogate uncertainty becomes more pronounced (see Section 4.1).

The compressor pressure ratio (PR_C), which governs both brake-specific fuel consumption and maximum cylinder pressure, is slightly lower than the baseline value (3.430 versus 3.700). Although a higher pressure ratio generally improves combustion efficiency by increasing intake-air density, the optimized value provides sufficient charge density to maintain efficient combustion while limiting peak cylinder pressure and avoiding unnecessarily high combustion temperatures. Combined with the slightly increased fuel mass per cycle (m_f = 0.3795 g/cycle), this calibration compensates for the modestly retarded injection timing, resulting in a net increase in brake power despite the substantial reduction in NO_x emissions.

Overall, the selected operating point illustrates the complementary roles of the three calibration variables. The start of injection primarily governs pollutant formation, the compressor pressure ratio regulates combustion efficiency and mechanical loading, and the fuel mass per cycle controls the available energy input. Simultaneous optimization of these interacting variables enables the proposed framework to identify a balanced operating condition that would be difficult to obtain through sequential or single-parameter calibration.

The resulting calibration therefore represents a physically meaningful compromise between combustion efficiency, engine performance, and pollutant formation. Rather than maximizing a single objective, the proposed tri-objective optimization framework identifies an operating point that effectively balances these competing requirements under representative Arctic operating conditions.

4.3. Algorithm Comparison

The comparison of four optimization paradigms was motivated by the No Free Lunch theorem (Section 2.4.2), which states that no optimization algorithm is universally superior across all optimization problems [55]. Accordingly, this study evaluated representative evolutionary (NSGA-II and GA), swarm-based (GWO), and Bayesian sequential (BO-GP) optimization strategies to assess the robustness of the proposed surrogate-assisted calibration framework rather than identify a universally optimal algorithm.

Despite their fundamentally different search mechanisms, all four algorithms converged toward similar regions of the Pareto front, producing comparable optimal values for brake power, brake-specific fuel consumption, and NO_x emissions (Tables 7 and 8). NSGA-II achieved the largest hypervolume, indicating the most complete approximation of the Pareto front, while GWO and the classical GA produced closely comparable results. BO-GP yielded a slightly lower hypervolume, primarily because of its intentionally smaller evaluation budget rather than an inherent limitation of the optimization strategy. Furthermore, no single algorithm consistently outperformed the others across all three objectives, reinforcing the practical implication of the No Free Lunch theorem: an algorithm's relative performance depends on the problem characteristics and the performance criteria considered.

The BO-GP results merit particular attention because they illustrate the trade-off between optimization quality and computational efficiency. Although its Pareto front was slightly less extensive than those from the population-based methods, BO-GP identified solutions close to the global best values. Relative to the best solutions obtained on the combined Pareto front, the differences were limited to 2.0% for brake power, 0.5% for BSFC, and 2.6% for NO_x emissions (Table 8 and Appendix C). These modest differences indicate that BO-GP successfully explored the relevant regions of the design space despite using substantially fewer objective-function evaluations.

This observation is particularly significant given the computational cost of high-fidelity engine simulations. BO-GP achieved 93.5% of the hypervolume obtained by NSGA-II while requiring only 150 surrogate evaluations, compared with 60,000 for NSGA-II and approximately 8000 for both GA and GWO (Table 2). On a hypervolume-per-evaluation basis, BO-GP is therefore substantially more sample-efficient than the population-based algorithms. Although this study used pre-trained Gaussian Process surrogates, this efficiency would be especially valuable when optimization is performed directly on a computationally expensive high-fidelity model. Given that each Diesel-RK simulation required approximately 36–42 s, direct optimization would require approximately 25–29 days for NSGA-II, 3.6 days for GA and GWO, but only 1.5–1.75 h for ^{2}BO-GP. Consequently, while population-based algorithms provide the most comprehensive approximation of the Pareto front, Bayesian optimization represents an attractive alternative when the evaluation budget is severely constrained or when surrogate models must be generated or updated adaptively.

Because we evaluated the four optimizers with different computational budgets and single runs, the comparison should not be taken as definitive evidence of intrinsic algorithmic superiority. The reported differences reflect performance under the computational settings used in this study. Future work will include repeated independent runs with harmonized computational budgets to enable a statistically rigorous comparison of algorithm performance.

Overall, the comparison demonstrates that the proposed surrogate-assisted optimization framework is robust across fundamentally different optimization paradigms. The close agreement among the resulting Pareto fronts indicates that the identified trade-offs primarily reflect the underlying engine-response characteristics rather than the behavior of a particular optimization algorithm.

4.4. Value of Tri-Objective Optimization over Single-Objective Optimization

The comparison with the native Diesel-RK single-objective optimizer (Section 3.10) provides an independent, high-fidelity assessment of the proposed framework, free from surrogate-model influences. Unlike the proposed methodology, which simultaneously considers brake power, brake-specific fuel consumption, and NO_x emissions, the native Diesel-RK optimizer improves only one objective at a time.

Optimizing either BSFC or BMEP produces only marginal improvements in engine performance and fuel efficiency (less than 1% relative to the Arctic baseline). However, these gains are accompanied by substantial increases in NO_x emissions of 25–38%, reflecting no penalty on pollutant formation. Conversely, optimizing the composite emission index (SE) reduces NO_x emissions by 64.6%, but only at the expense of a 7.1% reduction in brake power and a 7.6% increase in brake-specific fuel consumption. These results clearly illustrate the inherent conflict among the three performance objectives and demonstrate that optimizing a single criterion inevitably shifts the solution toward one extreme of the trade-off space.

In contrast, the SIMUS-selected operating point K, obtained through the proposed tri-objective optimization framework, simultaneously increases brake power by 3.7%, limits the increase in brake-specific fuel consumption to only 0.87%, and reduces NO_x emissions by 26.9% relative to the Arctic baseline. Although none of these individual improvements is optimal in isolation, achieving them simultaneously represents the most balanced engineering solution identified within the feasible operating domain.

Because this comparison relies entirely on direct Diesel-RK simulations rather than surrogate predictions, it independently validates the proposed methodology. More importantly, it shows that the framework's principal value lies not in the optimization algorithm itself but in explicitly formulating engine calibration as a tri-objective optimization problem.

By simultaneously considering engine performance, fuel efficiency, and emissions, the proposed framework identifies balanced operating conditions that conventional single-objective optimization cannot obtain by construction.

4.5. Limitations

The proposed framework focuses on optimizing pneumatic hybridization at the engine calibration level, where compressed air is represented through the compressor pressure ratio and its influence on in-cylinder combustion. Consequently, the upstream subsystems responsible for compressed air generation, storage, and delivery, including compressor performance, compressed air energy storage (CAES), and supervisory energy management, are beyond the scope of the present work. Integrating these system-level components with the engine-level optimization constitutes a natural extension of the proposed methodology.

The comparison with the native Diesel-RK optimizer (Section 3.10) should also be interpreted within its intended context. The composite emission index (SE) includes a particulate matter (PM) component that was neither independently modeled nor incorporated into the Gaussian Process surrogate framework. Consequently, the SE-optimal operating point should be regarded as a high-fidelity Diesel-RK reference for comparison with the proposed methodology rather than as a surrogate-validated operating condition.

Although the Gaussian Process surrogates demonstrate excellent predictive performance for brake power, brake-specific fuel consumption, and maximum cylinder pressure, the predictive accuracy for NO_x emissions remains more variable across the design space. The global sensitivity analysis indicates that this behavior is primarily associated with the strong nonlinear influence of the start of injection on thermal NO_x formation. Accordingly, candidate operating points selected from the surrogate-derived Pareto front should be confirmed through high-fidelity simulations and interpreted alongside their associated predictive uncertainty before adoption as final calibration solutions, as demonstrated for the selected operating point K.

Experimental NO_x measurements were not available for the specific CAT 3516 configuration considered in this study. The manufacturer data used for engine-model validation provide power, torque, and BSFC information but no corresponding NO_x measurements. Consequently, the reported NO_x results remain model-based engine-out predictions, and future work requires experimental validation of the predicted NO_x response.

Finally, we established the optimization domain and the associated convex-hull safeguard through dedicated Diesel-RK parametric analyses rather than arbitrary assumptions. Nevertheless, the lower bound of the fuel mass per cycle (m_f) was verified only at the most demanding operating condition, rather than through a complete boundary exploration. Although no physically meaningful operating points were identified below the adopted limit, additional feasible regions outside the selected design space cannot be completely excluded. The quantitative optimum obtained in this study is specific to the CAT 3516 configuration and the Arctic operating conditions considered and therefore requires engine-specific validation before being applied to other systems. However, the observed trade-offs among pneumatic assistance, brake power, BSFC, NO_x, and cylinder pressure may extend to other diesel-generator applications. After appropriate model validation, constraint definition, and surrogate retraining, the proposed framework can also be applied to other engines and operating environments.

The present results should be interpreted within the engine-level scope of the study. Experimental NO_x measurements were not available for the specific CAT 3516 configuration, and the analysis did not include the energy required for compressed air generation, cooling, CAES, and distribution. In addition, the optimizer comparison used different computational budgets and single runs, and the numerical optimum remains specific to the

investigated engine and Arctic operating conditions. Future work should therefore include experimental validation of the predicted NO_x response at the optimized operating point, repeated optimizer evaluations under harmonized computational budgets, integration of the complete compressed air energy chain, and system-level energetic, economic, and environmental assessment.

Future work will extend the present framework by coupling the engine-level optimization with detailed models of compressed air generation, storage, and energy management within complete wind–diesel–CAES hybrid systems. Additional research will also investigate adaptive sampling strategies and enhanced surrogate formulations to further improve predictive accuracy in highly nonlinear regions of the design space, particularly for NO_x emissions.

5. Conclusions

This study developed and numerically validated an integrated surrogate-assisted tri-objective optimization framework for calibrating a pneumatically hybridized CAT 3516 diesel generator operating under representative Arctic conditions at Raglan Mine. The framework combines high-fidelity Diesel-RK thermodynamic simulations, adaptive Sobol-based design of experiments, Gaussian Process surrogate modeling, global sensitivity analysis, multi-objective optimization, objective Pareto-front ranking using SIMUS, and independent high-fidelity validation within a unified computational workflow.

The Gaussian Process surrogate models accurately reproduced the high-fidelity Diesel-RK simulations, achieving coefficients of determination greater than 0.97 for brake power, brake-specific fuel consumption, and maximum cylinder pressure. Although the NO_x surrogate exhibited lower predictive accuracy ($R^2 = 0.82$), the global sensitivity analysis demonstrated that this limitation primarily reflects the strong nonlinear dependence of thermal NO_x formation on the start of injection rather than deficiencies in the surrogate modeling approach. More importantly, the proposed framework systematically incorporated predictive uncertainty throughout the calibration process, allowing candidate operating points to be evaluated not only by predicted performance but also by the confidence associated with those predictions.

Among the 284 Pareto-optimal solutions generated by the four optimization algorithms, the SIMUS multicriteria decision-making procedure consistently identified the same operating point using two independent ranking methods. Independent high-fidelity Diesel-RK validation confirmed that the selected operating point increased brake power by 3.7%, reduced NO_x emissions by 26.9%, and incurred only a 0.87% increase in brake-specific fuel consumption relative to the Arctic baseline. All validated outputs remained within the Gaussian Process 95% predictive intervals, demonstrating both the accuracy of the surrogate predictions and the reliability of the associated uncertainty estimates.

Comparison with the native Diesel-RK single-objective optimizer further demonstrated the value of the proposed tri-objective formulation. While optimizing a single performance criterion improved that objective, it consistently produced undesirable trade-offs in the remaining objectives. In contrast, the proposed framework identified a balanced operating condition that improved engine performance while substantially reducing emissions, illustrating the advantage of explicitly considering competing objectives during engine calibration.

From an engineering perspective, the proposed calibration strategy can be implemented through engine control software without modifying the existing engine hardware, providing a practical pathway to improve the environmental performance of pneumatically hybridized diesel generators operating in isolated Arctic microgrids. Although the present validation was performed entirely through high-fidelity numerical simulations, the next

stage of this research should involve experimental implementation and field validation on a full-scale CAT 3516 engine operating under representative Arctic conditions.

The reported improvements should therefore be interpreted as engine-level results under pneumatic assistance and not as the net performance of the complete wind–compressed air–diesel energy system.

Future work will extend the framework beyond engine calibration by integrating compressed air generation, storage, and supervisory energy management into a unified optimization of complete wind–diesel–CAES hybrid systems. Additional developments will focus on improving surrogate modeling in highly nonlinear combustion regimes, particularly for NO_x prediction, and on extending the methodology to multi-engine optimization and additional environmental performance indicators.

Beyond the specific application to pneumatic assistance, the proposed framework provides a general methodology for surrogate-assisted calibration of computationally expensive diesel-engine optimization problems.

Author Contributions: J.K.B.: Conceptualization, Data curation, Formal analysis, Investigation, Methodology, Project administration, Resources, Software, Validation, Visualization, Writing—original draft, Writing—review and editing. E.K.T.: Conceptualization, Data curation, Formal analysis, Investigation, Methodology, Project administration, Resources, Software, Validation, Visualization, Writing—original draft, Writing—review and editing. D.R.R.: Conceptualization, Investigation, Methodology, Project administration, Resources, Writing—review and editing. A.I.: Conceptualization, Data curation, Formal analysis, Investigation, Methodology, Project administration, Resources, Software, Validation, Visualization, Writing—original draft, Writing—review and editing. All authors have read and agreed to the published version of the manuscript.

Funding: The authors acknowledge the financial contributions from NSERC (grants RGPIN-4220/2019 and RGPIN-2025-04831), FRQNT (grants 322720, 340327, and 364164), and the Michel Trottier private donation to the L3e research group.

Data Availability Statement: The original contributions presented in this study are included in the article. Further inquiries can be directed to the corresponding author.

Acknowledgments: The authors acknowledge using ChatGPT (GPT-6, OpenAI) to assist with the graphical preparation of Figure 1. The authors reviewed and approved the final figure and take full responsibility for its scientific content. After using these tools, the authors carefully reviewed, revised, and verified all generated content and take full responsibility for the accuracy, integrity, and originality of the published work. During the preparation of this manuscript, the authors used generative AI and AI-assisted language technologies to improve the clarity of expression, grammar, style, and overall presentation of the manuscript. In particular, ChatGPT (OpenAI), Grammarly (www.grammarly.com), and Antidote (www.antidote.info) were used exclusively to assist with language editing, text refinement, and manuscript organization. These tools were not used to generate scientific results, perform data analysis, interpret findings, or draw scientific conclusions.

Conflicts of Interest: The authors declare no conflicts of interest.

Appendix A. Performance Curves of Caterpillar 3516

CAT

3516
Industrial Engine

PERFORMANCE CURVES

1492 bkW/2000 bhp @ 1800 rpm

IND - C (Intermittent) - TM3382-08

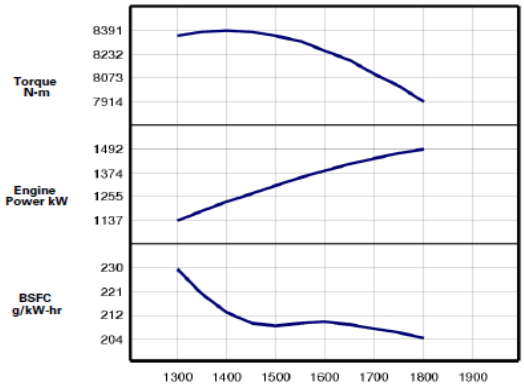

Engine Speed rpm	Engine Power kW	Torque N-m	BSFC g/kW-hr	Fuel Rate L/hr
1800	1492	7914	204	362.8
1750	1469	8017	206	360.8
1700	1443	8106	207.9	357.7
1650	1415	8188	209.4	353.3
1600	1384	8259	210	346.3
1550	1350	8315	209.5	336.7
1500	1313	8358	208.9	326.8
1450	1273	8381	209.9	318.5
1400	1230	8391	213.8	313.5
1350	1185	8381	220.5	311.2
1300	1137	8353	229.5	311.1

3 13 April 2012 1:44 PM

Appendix B. Dataset 155 Points

ID	(°BTDC)	- PRc	m_f (g/Cycle)	P_{eng} (kW)	BSFC (g/kWh)	NO_x (g/kWh)	p_{max} (bar)	Feasible	Source
1	12.034	3.536	0.3589	1476.7	209.99	5.054	140.67	1	Sobol_base
2	6.748	3.536	0.3589	1458.3	212.64	4.061	129.32	1	Sobol_base
3	12.034	2.245	0.3589	1435.3	216.05	4.468	100.73	1	Sobol_base
4	12.034	3.536	0.3634	1514.1	207.37	6.017	145.68	1	Sobol_base
5	6.748	2.245	0.3634	1396.5	224.83	2.567	87.771	1	Sobol_base
6	18.771	1.933	0.284	1143.9	214.51	8.741	103.87	1	Sobol_base
7	15.706	1.933	0.284	1140.6	215.13	6.84	96.968	1	Sobol_base
8	18.771	3.721	0.284	1115.6	219.95	10.437	172.01	1	Sobol_base
9	18.771	1.933	0.2999	1205.4	214.96	8.531	104.19	1	Sobol_base
10	15.706	3.721	0.2999	1201.7	215.63	8.229	162.9	1	Sobol_base
11	13.19	2.822	0.344	1411.7	210.53	5.2295	119.57	1	Sobol_base
12	11.533	2.822	0.344	1421.7	209.06	5.3869	119.74	1	Sobol_base
13	13.19	3.144	0.344	1435	207.12	6.4461	136.03	1	Sobol_base

https://doi.org/10.3390/en19204855

ID	(°BTDC)	- PRc	m_f (g/Cycle)	P_{eng} (kW)	BSFC (g/kWh)	NO_x (g/kWh)	p_{max} (bar)	Feasible	Source
14	13.19	2.822	0.2527	1017.9	214.49	6.6516	122.99	1	Sobol_base
15	11.533	3.144	0.2527	998.21	218.72	5.7701	128.73	1	Sobol_base
16	6.254	2.704	0.2821	1127.3	216.2	3.7321	100.61	1	Sobol_base
17	17.921	2.704	0.2821	1159.9	210.14	9.7691	134.27	1	Sobol_base
18	6.254	1.571	0.2821	1021.9	238.51	2.4904	63.94	1	Sobol_base
19	6.254	2.704	0.3242	1295.8	216.17	3.3754	100.61	1	Sobol_base
20	17.921	1.571	0.3242	1223.7	228.91	6.8363	86.647	1	Sobol_base
21	7.981	3.179	0.303	1210.2	216.33	3.7198	116.95	1	Sobol_base
22	18.514	3.179	0.303	1247	209.94	10.299	154.69	1	Sobol_base
23	7.981	2.063	0.303	1185.5	220.82	3.34	84.138	1	Sobol_base
24	7.981	3.179	0.3796	1547.2	211.98	3.6963	121.22	1	Sobol_base
25	18.514	2.063	0.3796	1513	216.77	7.5465	111.26	1	Sobol_base
26	14.964	2.357	0.3736	1520.4	212.3	5.8504	113.17	1	Sobol_base
27	10.813	2.357	0.3736	1490.6	216.55	3.9184	101.67	1	Sobol_base
28	14.964	2.97	0.3736	1565.4	206.2	6.955	135.92	1	Sobol_base
29	14.964	2.357	0.3156	1296.8	210.26	6.8624	112.58	1	Sobol_base
30	10.813	2.97	0.3156	1299.1	209.9	5.4841	122.4	1	Sobol_base
31	16.998	3.97	0.2631	977.8	232.48	7.4261	166.68	1	Sobol_base
32	13.674	3.97	0.2631	983.29	231.18	6.5151	161.58	1	Sobol_base
33	16.998	3.663	0.2631	1013	224.41	8.9716	162.5	1	Sobol_base
34	16.998	3.97	0.271	1024.8	228.47	8.7453	173.17	1	Sobol_base
35	13.674	3.663	0.271	1057.8	221.35	6.8829	152.03	1	Sobol_base
36	10.308	1.508	0.3292	1165.1	244.12	3.2234	69.555	1	Sobol_base
37	8.653	1.508	0.3292	1146.4	248.1	2.6881	66.38	1	Sobol_base
38	10.308	2.619	0.3292	1344.6	211.54	4.7938	109.15	1	Sobol_base
39	10.308	1.508	0.342	1195.3	247.2	2.9694	69.839	1	Sobol_base
40	8.653	2.619	0.342	1380.9	213.98	3.7846	104.22	1	Sobol_base
41	10.455	3	0.2556	1008.9	218.9	4.4424	116.58	1	Sobol_base
42	9.546	3	0.2556	1017.8	216.99	4.9934	118.46	1	Sobol_base
43	10.455	3.913	0.2556	942.24	234.38	4.9168	149.56	1	Sobol_base
44	10.455	3	0.3292	1356.2	209.72	5.1193	121.88	1	Sobol_base
45	9.546	3.913	0.3292	1324.1	214.81	4.9659	149.11	1	Sobol_base
46	17.74	2.493	0.3198	1325	208.54	8.7434	126.04	1	Sobol_base
47	19.784	2.493	0.3198	1323.9	208.71	10.165	131.86	1	Sobol_base
48	17.74	2.361	0.3198	1318.5	209.56	8.5148	120.71	1	Sobol_base
49	17.74	2.493	0.2666	1089	211.53	9.3762	124.57	1	Sobol_base
50	19.784	2.361	0.2666	1085.9	212.12	10.596	124.19	1	Sobol_base
51	16.3	3.517	0.3127	1275	211.9	7.2601	151.77	1	Sobol_base
52	8.206	3.517	0.3127	1260.6	214.32	4.5862	132.17	1	Sobol_base
53	16.3	1.688	0.3127	1210.7	223.15	6.2565	88.158	1	Sobol_base
54	16.3	3.517	0.2859	1145.7	215.6	8.5174	156.84	1	Sobol_base
55	8.206	1.688	0.2859	1075	229.79	3.0998	71.547	1	Sobol_base
56	9.255	1.995	0.3808	1426.2	230.7	3.0204	85.139	1	Sobol_base
57	14.123	1.995	0.3808	1480.1	222.29	4.9954	97.235	1	Sobol_base
58	9.255	3.337	0.3808	1568	209.83	4.5072	129.98	1	Sobol_base
59	9.255	1.995	0.3584	1365.4	226.8	3.1527	85.176	1	Sobol_base

ID	(°BTDC)	- PRc	m_f (g/Cycle)	P_{eng} (kW)	BSFC (g/kWh)	NO_x (g/kWh)	p_{max} (bar)	Feasible	Source
60	14.123	3.337	0.3584	1502.5	206.09	7.0088	146.2	1	Sobol_base
61	7.481	3.707	0.3346	1328	217.68	3.4765	131.77	1	Sobol_base
62	15.278	3.707	0.3346	1379.5	209.57	7.7082	161.78	1	Sobol_base
63	7.481	2.779	0.3346	1351.4	213.92	3.7355	106.33	1	Sobol_base
64	7.481	1.795	0.3454	1261.9	236.49	2.5709	74.153	1	Sobol_base
65	15.278	1.795	0.3454	1333.5	223.78	5.6289	91.132	1	Sobol_base
66	14.574	1.948	0.2746	1101.8	215.34	6.3461	94.536	1	Sobol_base
67	7.174	1.795	0.2746	1047.9	226.4	3.0434	73.193	1	Sobol_base
68	14.574	1.948	0.2746	1101.7	215.36	6.3479	94.53	1	Sobol_base
69	14.574	1.795	0.2824	1116.9	218.45	5.9676	88.588	1	Sobol_base
70	7.174	1.948	0.2824	1092.9	223.24	3.1742	78.198	1	Sobol_base
71	19.465	3.269	0.3661	1534.5	206.13	8.8441	155.04	1	Sobol_base
72	16.563	3.269	0.3661	1543	205	8.3684	152.27	1	Sobol_base
73	19.465	2.504	0.3661	1517.1	208.5	8.9654	132.01	1	Sobol_base
74	19.465	3.269	0.3043	1247.2	210.8	10.895	160.44	1	Sobol_base
75	16.563	2.504	0.3043	1257.6	209.07	8.1342	122.56	1	Sobol_base
76	12.229	2.215	0.2938	1190.2	213.28	5.4194	99.348	1	Sobol_base
77	12.889	2.215	0.2938	1192.6	212.85	5.6987	100.86	1	Sobol_base
78	12.229	3.472	0.2938	1186	214.03	6.0899	142.64	1	Sobol_base
79	12.229	2.215	0.3762	1490.4	218.08	4.3015	100.41	1	Sobol_base
80	12.889	3.472	0.3762	1575.2	206.35	6.2697	145.96	1	Sobol_base
81	12.603	3.302	0.3256	1335.6	210.62	5.3914	134.16	1	Sobol_base
82	13.406	3.302	0.3256	1349.8	208.42	6.7926	142.26	1	Sobol_base
83	12.603	1.641	0.3256	1219.7	230.64	4.3774	79.066	1	Sobol_base
84	12.603	3.302	0.277	1112.2	215.18	6.3357	137.84	1	Sobol_base
85	13.406	1.641	0.277	1070.9	223.48	5.1647	79.685	1	Sobol_base
86	19.966	2.17	0.2508	1012.3	214.06	10.509	115.42	1	Sobol_base
87	9.266	2.17	0.2508	999.63	216.77	4.4043	89.826	1	Sobol_base
88	19.966	3.075	0.2508	985.29	219.93	11.509	150.29	1	Sobol_base
89	19.966	2.17	0.3486	1418.2	212.38	9.0882	119.05	1	Sobol_base
90	9.266	3.075	0.3486	1431.9	210.34	4.6044	121.27	1	Sobol_base
91	14.179	3.84	0.3782	1566.6	208.58	5.916	157.12	1	Sobol_base
92	19.121	3.84	0.3782	1586.4	205.97	10.388	182.99	0	Sobol_base
93	14.179	3.788	0.3782	1585.2	206.14	7.0894	161.8	1	Sobol_base
94	14.179	3.84	0.3688	1537.6	207.23	7.0862	163.29	1	Sobol_base
95	19.121	3.788	0.3688	1543.5	206.45	10.433	180.85	0	Sobol_base
96	7.001	1.693	0.3163	1154.9	236.63	2.6196	69.794	1	Sobol_base
97	10.551	1.693	0.3163	1188.7	229.9	3.668	76.797	1	Sobol_base
98	7.001	2.178	0.3163	1235.8	221.13	3.0234	85.686	1	Sobol_base
99	7.001	1.693	0.3053	1123.5	234.77	2.6628	69.637	1	Sobol_base
100	10.551	2.178	0.3053	1223.7	215.56	4.5233	94.164	1	Sobol_base
101	8.782	3.405	0.2698	1048.8	222.27	3.9312	125.22	1	Sobol_base
102	12.02	3.405	0.2698	1068.7	218.13	6.0255	139.01	1	Sobol_base
103	8.782	2.706	0.2698	1088.8	214.09	4.7106	107.46	1	Sobol_base
104	8.782	3.405	0.2593	1008.1	222.25	4.5894	129.05	1	Sobol_base
105	12.02	2.706	0.2593	1050.6	213.24	6.08	116.01	1	Sobol_base

ID	(°BTDC)	- PRc	m_f (g/Cycle)	P_{eng} (kW)	BSFC (g/kWh)	NO_x (g/kWh)	p_{max} (bar)	Feasible	Source
106	15.899	2.117	0.3404	1373.7	214.09	6.4993	105.58	1	Sobol_base
107	17.526	2.117	0.3404	1379.1	213.26	7.5625	110.32	1	Sobol_base
108	15.899	3.577	0.3404	1414.4	207.94	8.2165	160.01	1	Sobol_base
109	15.899	2.117	0.3302	1336.6	213.44	6.5935	105.41	1	Sobol_base
110	17.526	3.577	0.3302	1364.3	209.11	9.4867	166.09	1	Sobol_base
111	18.247	2.945	0.2974	1223.8	209.96	8.7082	138.6	1	Sobol_base
112	6.36	2.945	0.2974	1195.7	214.9	3.9996	109.1	1	Sobol_base
113	18.247	3.059	0.2974	1224.2	209.89	10.079	148.89	1	Sobol_base
114	18.247	2.517	0.3531	1464.8	208.28	8.4165	128.67	1	Sobol_base
115	6.36	2.517	0.3531	1391.5	219.25	2.7974	95.391	1	Sobol_base
116	10.823	1.974	0.3635	1393.6	225.36	3.6842	88.155	1	Sobol_base
117	16.187	2.517	0.3635	1502.5	209.03	6.9537	122.78	1	Sobol_base
118	10.823	1.974	0.3635	1393.4	225.4	3.684	88.137	1	Sobol_base
119	10.823	2.517	0.2891	1178.6	211.94	5.2084	106.56	1	Sobol_base
120	16.187	1.974	0.2891	1164.8	214.44	7.1563	99.782	1	Sobol_base
121	18.247	3.857	0.2899	1136.7	220.35	8.4777	168.15	1	Sobol_base
122	6.36	3.857	0.2899	1113.6	224.92	3.808	136.42	1	Sobol_base
123	18.247	3.27	0.2899	1177.4	212.73	10.009	155.33	1	Sobol_base
124	18.247	3.857	0.3104	1242.7	215.81	9.8683	176.26	1	Sobol_base
125	6.36	3.27	0.3104	1253.8	213.9	4.0046	119.17	1	Sobol_base
126	10.823	1.63	0.3541	1273.9	240.17	3.3744	75.233	1	Sobol_base
127	16.187	1.63	0.3541	1316.4	232.4	5.6012	86.442	1	Sobol_base
128	10.823	1.755	0.3541	1311.5	233.27	3.5114	79.802	1	Sobol_base
129	6.453	1.592	0.2542	952.22	230.65	1.9403	64.912	1	Targeted_LHS_enrichment
130	8.318	2.315	0.3286	1332.4	213.08	3.0111	96.665	1	Targeted_LHS_enrichment
131	6.913	2.019	0.3469	1351.8	221.73	2.1698	84.316	1	Targeted_LHS_enrichment
132	7.618	2.099	0.314	1253.5	216.43	2.7059	87.737	1	Targeted_LHS_enrichment
133	7.941	1.781	0.2713	1066.3	219.82	2.8494	77.107	1	Targeted_LHS_enrichment
134	6.183	2.444	0.3782	1499.9	217.86	1.9995	95.535	1	Targeted_LHS_enrichment
135	8.721	1.879	0.2981	1182.2	217.87	2.9068	82.92	1	Targeted_LHS_enrichment
136	13.646	3.241	0.3305	1381.9	206.64	5.4311	143.6	1	Targeted_LHS_enrichment
137	14.015	3.432	0.3761	1591.8	204.14	5.6448	152.65	1	Targeted_LHS_enrichment
138	12.904	3.344	0.308	1265.1	210.35	5.0809	143.97	1	Targeted_LHS_enrichment
139	14.896	2.889	0.2626	1062.9	213.47	4.976	127.13	1	Targeted_LHS_enrichment
140	14.237	2.946	0.3479	1470.6	204.39	5.7106	135.99	1	Targeted_LHS_enrichment
141	12.431	3.108	0.2854	1165.6	211.55	4.7794	133.54	1	Targeted_LHS_enrichment
142	12.176	3.027	0.2901	1191	210.45	4.7604	130.42	1	Targeted_LHS_enrichment
143	7.054	3.698	0.3622	1469	213.03	2.7908	136.27	1	Targeted_LHS_enrichment
144	6.04	3.867	0.3251	1274	220.48	2.6284	137.65	1	Targeted_LHS_enrichment
145	7.346	3.738	0.275	1040	228.46	2.7452	136.97	1	Targeted_LHS_enrichment
146	6.732	3.966	0.3322	1304.3	220.06	2.7484	142.97	1	Targeted_LHS_enrichment
147	6.446	3.574	0.379	1544.2	212.06	2.1851	130.63	1	Targeted_LHS_enrichment
148	7.682	3.553	0.3068	1219.6	217.34	3.0834	132.82	1	Targeted_LHS_enrichment

ID	(°BTDC)	- PRc	m_f (g/Cycle)	P_{eng} (kW)	BSFC (g/kWh)	NO_x (g/kWh)	p_{max} (bar)	Feasible	Source
149	7.737	3.811	0.2655	973.1	235.73	2.2514	136.08	1	Targeted_LHS_enrichment
150	18.054	3.021	0.3576	1522	203	7.7987	151.7	1	Targeted_LHS_enrichment
151	19.292	2.975	0.2555	1018.5	216.74	8.3789	147.15	1	Targeted_LHS_enrichment
152	18.755	3.172	0.303	1253.8	208.79	8.4681	157.41	1	Targeted_LHS_enrichment
153	18.392	3.129	0.3279	1378.6	205.5	8.3024	156.5	1	Targeted_LHS_enrichment
154	19.748	2.812	0.2901	1202.9	208.38	9.2885	147.02	1	Targeted_LHS_enrichment
155	19.505	2.909	0.379	1614.7	202.79	8.5032	153.64	1	Targeted_LHS_enrichment

Appendix C. Combined Pareto Front 284 Points with Algorithms

SOI (°BTDC)	PRc	m_f (g/Cycle)	$\bar{P}_{eng}$ (kW)	BSFC (g/kWh)	NO_x (g/kWh)	Algorithm	Selected Point
18.41521053	3.055004412	0.378944612	1606.361426	203.6093438	8.24946026	NSGA-II	
18.60315729	3.054783104	0.378856684	1606.33081	203.5661078	8.352091935	GA	
18.82566056	3.027910265	0.37885664	1606.283591	203.4963133	8.469932239	GA	
18.55694214	3.052837221	0.378848425	1606.187666	203.5736622	8.327351266	GA	
18.65187256	3.006271279	0.378965437	1606.00806	203.5397302	8.376929192	NSGA-II	
18.31673104	3.022172554	0.378941264	1605.586868	203.6215688	8.195540892	NSGA-II	
17.83868249	3.087285281	0.378914323	1605.448063	203.8057537	7.928522085	GA	
18.0438366	3.029735367	0.378961004	1605.227544	203.7022058	8.043711229	NSGA-II	
18.70451757	3.031712129	0.37848044	1604.572357	203.5210811	8.410346376	NSGA-II	
17.6447667	3.03541396	0.378944612	1604.303533	203.8380164	7.817896884	NSGA-II	
17.5426315	3.185360194	0.378565766	1603.791755	204.1260894	7.763149123	GWO	
16.6327866	3.13770224	0.379148483	1603.692613	204.300565	7.235454173	GA	
17.31395012	3.058238257	0.378884661	1603.589326	203.9607516	7.628820519	NSGA-II	
16.44292369	3.095166173	0.379384119	1603.579262	204.352766	7.125560043	GA	
18.14865461	3.026739429	0.378437511	1603.216235	203.665352	8.107784809	NSGA-II	
15.97483106	3.133410548	0.379392662	1602.468157	204.5944596	6.862880893	NSGA-II	
15.80446797	3.094812222	0.379567062	1602.017295	204.6887991	6.767595349	NSGA-II	
15.63153619	3.094493605	0.379513707	1601.106059	204.7885685	6.673413504	NSGA-II	
17.26301211	3.024819986	0.378432488	1600.894788	203.9953063	7.603685637	NSGA-II	
16.86405619	3.066472695	0.378523277	1600.893888	204.1476111	7.373174225	NSGA-II	
15.51077979	3.094530963	0.379517293	1600.630183	204.8608343	6.607904133	NSGA-II	
15.51077979	3.094530963	0.379507956	1600.591364	204.8607356	6.607966122	NSGA-II	
16.69550582	3.066472695	0.378523277	1600.357356	204.2255548	7.276469978	NSGA-II	
15.29082572	3.08830284	0.37957234	1599.817209	205.0056286	6.489393384	NSGA-II	
15.21096585	3.094812222	0.379567062	1599.57296	205.0486335	6.4468752	NSGA-II	
15.45506218	3.185436082	0.379016969	1599.397561	204.8826573	6.581127679	GWO	
17.36927793	3.023750456	0.377987425	1599.31727	203.9459291	7.669026758	NSGA-II	
15.45509763	3.18461261	0.378995502	1599.301909	204.8821932	6.581287961	GWO	
15.3883792	3.182787942	0.378985499	1598.987578	204.9156919	6.545432623	GWO	
16.40621543	3.101500374	0.378211975	1598.636898	204.3627785	7.113979077	NSGA-II	

SOI (°BTDC)	PRc	m_f (g/Cycle)	$\bar{P}_{eng}$ (kW)	BSFC (g/kWh)	NO_x (g/kWh)	Algorithm	Selected Point
15.49474268	3.145045986	0.378852577	1598.511089	204.8468468	6.603642037	GWO	
15.0424729	3.292509219	0.379117738	1598.400222	205.13985	6.360421022	NSGA-II	
15.447796	3.181907811	0.378778	1598.338892	204.8844333	6.578778958	GWO	
15.02718126	3.215222599	0.379107555	1598.240303	205.1177344	6.352416135	GWO	
15.33431296	3.099336254	0.379092123	1598.207989	204.9604791	6.515733129	GWO	
14.48204761	3.18672611	0.379600783	1597.7267	205.4423265	6.065286738	GWO	
14.53162397	3.306677558	0.379372359	1597.390483	205.3885581	6.092214675	NSGA-II	
15.18523428	3.082154907	0.379117738	1597.347898	205.0778757	6.436025896	NSGA-II	
16.18182973	3.058127983	0.378258972	1597.313193	204.4928546	6.98683751	NSGA-II	
14.42598414	3.218682591	0.379419582	1596.966722	205.4618542	6.037380908	NSGA-II	
14.88469455	3.256099244	0.378885126	1596.828616	205.2047063	6.278850247	NSGA-II	
19.22022429	3.024003062	0.376463311	1596.715529	203.4141726	8.698868266	GA	
14.78907555	3.147423725	0.378996026	1596.151068	205.2674507	6.228166853	NSGA-II	
15.4691755	3.188895555	0.378174135	1595.912766	204.8781163	6.594299891	GWO	
15.70102503	3.132330434	0.378068955	1595.877954	204.7286689	6.72122722	NSGA-II	
15.42290462	3.175848533	0.378211427	1595.807782	204.8939481	6.56906735	GWO	
14.08989735	3.292509219	0.379418283	1595.661018	205.6351153	5.864611716	NSGA-II	
19.15430094	2.982737683	0.376404105	1595.554802	203.4339401	8.666631101	NSGA-II	
14.56353321	3.251179724	0.378893481	1595.502468	205.3764836	6.111482755	NSGA-II	
19.04271093	2.982737683	0.376404105	1595.386843	203.4556719	8.610135711	NSGA-II	
14.26727543	3.293143428	0.379117384	1595.186232	205.5358486	5.957343334	NSGA-II	
15.60286501	3.170936857	0.37790645	1595.174809	204.7984386	6.668675847	GWO	
14.38379357	3.256099244	0.378893481	1594.721576	205.4785973	6.018593135	NSGA-II	
13.93968205	3.306677558	0.379351194	1594.676077	205.7195765	5.788012238	NSGA-II	
14.01697873	3.394810024	0.379335236	1594.494204	205.6680322	5.827690058	GWO	
13.89987887	3.247025288	0.37937665	1594.463737	205.7790732	5.767497279	GWO	
13.99829554	3.374060718	0.379166733	1593.871501	205.6773277	5.819031434	NSGA-II	
15.47014506	3.187983438	0.377578987	1593.387705	204.8778611	6.598749836	GWO	
14.94668703	3.165804382	0.378084805	1593.227856	205.1590969	6.316241003	NSGA-II	
13.56280789	3.369872975	0.37939479	1592.875691	205.9250158	5.594954612	NSGA-II	
13.51498906	3.391602203	0.379384062	1592.453791	205.9525905	5.570549859	NSGA-II	
13.33278299	3.242180565	0.379580386	1592.39387	206.175673	5.476306575	GWO	
14.33429432	3.25349113	0.37835607	1592.212199	205.5121118	5.99609561	GWO	
13.40274832	3.392717588	0.379385177	1591.91324	206.0214041	5.513120069	NSGA-II	
15.51753497	3.170866429	0.377189816	1591.810877	204.841688	6.627033682	GWO	
13.28768608	3.35736726	0.379390146	1591.570015	206.1031094	5.454208048	NSGA-II	
15.97166794	3.069174851	0.377015686	1591.531826	204.5869017	6.878312404	GWO	
13.15570294	3.367119346	0.379536535	1591.486969	206.1829526	5.385883523	NSGA-II	
13.68443362	3.283982553	0.378748316	1590.879651	205.8984179	5.660585478	GWO	
13.8658085	3.352013597	0.378492391	1590.532493	205.7649755	5.754800043	GWO	

SOI (°BTDC)	PRc	m_f (g/Cycle)	$\bar{P}_{eng}$ (kW)	BSFC (g/kWh)	NO_x (g/kWh)	Algorithm	Selected Point
13.07707146	3.432732416	0.37950294	1590.454557	206.2325934	5.345784063	NSGA-II	
12.82813939	3.338733392	0.37967586	1590.424338	206.4276154	5.217366417	GWO	
13.01715055	3.264795577	0.379450746	1590.294635	206.379283	5.31535382	GWO	
12.75059423	3.294756974	0.379745409	1590.210466	206.5357588	5.177282626	GWO	
19.42886916	3.005605497	0.374912293	1590.053243	203.3758977	8.819122949	NSGA-II	
12.9407713	3.333503287	0.379385177	1589.800357	206.3562603	5.276551859	NSGA-II	
19.48877481	3.005605497	0.374828409	1589.76227	203.3689788	8.848757874	NSGA-II	
15.51822836	3.170565208	0.376690036	1589.686396	204.8413127	6.630736119	GWO	
19.48877481	3.000109521	0.374828409	1589.661076	203.3683698	8.848757869	NSGA-II	
12.93726658	3.409901288	0.379385177	1589.461234	206.3227714	5.274756031	NSGA-II	
19.26147311	2.994977509	0.374858931	1589.413716	203.400252	8.738090209	NSGA-II	
12.50103348	3.17740602	0.380136606	1589.175551	206.9652172	5.047533133	GWO	
12.64667968	3.278599699	0.379586384	1588.871184	206.6409563	5.124842821	GWO	
12.51213362	3.327797108	0.379669656	1588.637966	206.674401	5.055534013	GWO	
12.70613622	3.43004883	0.379508583	1588.612174	206.4802753	5.155692924	NSGA-II	K (SIMUS knee point)
12.85129206	3.414774573	0.379287327	1588.559514	206.3836874	5.231192003	NSGA-II	
12.42719126	3.285692265	0.379756533	1588.357922	206.8012076	5.011647228	GWO	
13.30845013	3.381712942	0.378602255	1588.18087	206.0987147	5.468907367	GWO	
12.98646819	3.360627817	0.378951189	1588.144171	206.3120941	5.30217331	GWO	
12.60425269	3.432234973	0.379507516	1588.048505	206.5520896	5.103506186	NSGA-II	
15.34169988	3.193506129	0.376429902	1588.025075	204.9501869	6.536868691	GWO	
14.64389794	3.171551692	0.377104169	1587.800784	205.3425318	6.163572721	GWO	
12.57052947	3.31173397	0.379349065	1587.579131	206.6545022	5.087026988	GWO	
12.52989089	3.369872975	0.37939479	1587.544655	206.6243457	5.065991759	NSGA-II	
13.24358391	3.413358275	0.3785827	1587.523459	206.1432835	5.435789334	GWO	
12.43811689	3.425339101	0.379508583	1587.218585	206.6700307	5.018464347	NSGA-II	
12.42659085	3.372537943	0.379438743	1587.147568	206.6985439	5.012915855	GWO	
14.67963196	3.269941747	0.376799233	1587.076084	205.3363988	6.183974603	NSGA-II	
14.67173969	3.165937376	0.376798918	1586.577222	205.3261116	6.179859908	GWO	
12.26983063	3.129921527	0.379970202	1586.126522	207.3085713	4.93021178	NSGA-II	
15.54262922	3.087030126	0.376003027	1585.892186	204.8155391	6.648611902	GWO	
12.29291487	3.42364254	0.379372122	1585.848335	206.7802973	4.944938901	NSGA-II	
12.14882662	3.405355406	0.379358207	1585.095396	206.8928305	4.871547166	NSGA-II	
11.62923252	3.26362814	0.380176339	1585.018252	207.5163966	4.605236052	GWO	
15.72115901	3.126974597	0.375485074	1584.948714	204.7060278	6.750105088	GWO	
14.74230377	3.253829568	0.376216333	1584.837102	205.3028839	6.220139754	GWO	
16.02100438	3.127164386	0.375177381	1584.739513	204.5516904	6.919299944	NSGA-II	
12.39573846	3.353234589	0.378809037	1584.329821	206.7497722	5.000263314	GWO	
11.83814007	3.399834294	0.379577298	1584.238891	207.1338326	4.712991103	GA	
11.98298484	3.46496027	0.379375156	1583.723595	207.0256646	4.787211458	NSGA-II	
11.539735	3.351348521	0.379818766	1583.482036	207.4254024	4.562318674	GWO	

SOI (°BTDC)	PRc	m_f (g/Cycle)	$\bar{P}_{eng}$ (kW)	BSFC (g/kWh)	NO_x (g/kWh)	Algorithm	Selected Point
11.76394096	3.321283671	0.379501214	1583.453583	207.2882818	4.675989584	GWO	
11.93069423	3.46496207	0.379373527	1583.418447	207.0657446	4.760736234	NSGA-II	
17.71104825	3.045564832	0.373833879	1583.039559	203.7804734	7.906283901	NSGA-II	
11.3633749	3.397478335	0.379965559	1582.984352	207.5174346	4.474370021	NSGA-II	
12.33936884	3.385383688	0.378562791	1582.875441	206.7748027	4.972669091	GWO	
15.37417548	3.114645392	0.37529959	1582.639448	204.8997258	6.561721118	GWO	
11.76697642	3.521143299	0.379438018	1581.96394	207.2486611	4.67782026	NSGA-II	
11.82599642	3.402506179	0.379021303	1581.7866	207.1550889	4.709552664	NSGA-II	
12.34439005	3.430664045	0.378324453	1581.582493	206.7711409	4.976417701	NSGA-II	
11.25519928	3.315386724	0.379811897	1581.477926	207.7358342	4.4220526	GWO	
14.97150664	3.13026371	0.375375543	1581.459321	205.1430808	6.345797554	GWO	
18.88497188	3.000182333	0.373075696	1581.334408	203.4631399	8.566625631	NSGA-II	
18.74623779	3.000182333	0.373075696	1581.107296	203.4921465	8.493182784	NSGA-II	
11.49051754	3.405355406	0.379289605	1580.882944	207.4208001	4.540375183	NSGA-II	
11.0892395	3.292553482	0.379950851	1580.786909	207.9342059	4.340869624	GWO	
11.5972773	3.44950139	0.379147517	1580.652479	207.3286686	4.594178422	NSGA-II	
18.36510991	3.000182333	0.373075696	1580.402501	203.5869456	8.28544554	NSGA-II	
10.94118903	3.436597634	0.380007967	1580.319273	207.8536142	4.26969043	GA	
12.36375818	3.404470842	0.377935523	1580.218265	206.765701	4.988251553	GWO	
10.92669787	3.436421062	0.37999298	1580.162718	207.8666055	4.262866733	NSGA-II	
11.12299593	3.413887514	0.379546245	1579.63042	207.7197237	4.359024982	NSGA-II	
11.06203145	3.425700484	0.379558148	1579.241612	207.7655442	4.329562899	NSGA-II	
16.40621543	3.101500374	0.373628093	1579.160247	204.3427501	7.150045307	NSGA-II	
10.70071205	3.331617031	0.380086446	1578.999475	208.1995742	4.156223327	GWO	
11.28099193	3.44950139	0.379147517	1578.723016	207.5879558	4.437757935	NSGA-II	
10.65943528	3.434646494	0.37999298	1578.41495	208.1011892	4.137493931	NSGA-II	
10.54009026	3.440228458	0.38010652	1578.071949	208.2017336	4.082134483	GWO	
10.78187432	3.39599842	0.379546515	1577.440045	208.0327955	4.196502287	NSGA-II	
10.78187432	3.432678231	0.379546515	1577.338549	208.0061905	4.196502327	NSGA-II	
10.41602782	3.46669851	0.379987944	1576.572491	208.3119306	4.026385014	NSGA-II	
10.56418022	3.499270079	0.379818725	1576.527385	208.2013912	4.094401452	NSGA-II	
10.62565203	3.459712397	0.379546515	1576.145462	208.1390959	4.123846649	NSGA-II	
11.42689735	3.422945586	0.378269116	1576.044871	207.492597	4.513695116	GWO	
10.58379065	3.423177669	0.379503808	1575.876595	208.1875538	4.10476838	GWO	
11.69325672	3.494507515	0.377987425	1575.707416	207.3214785	4.64777601	NSGA-II	
10.26104225	3.432247965	0.379987944	1575.699431	208.4602481	3.957242521	NSGA-II	
10.26104225	3.432874798	0.379981593	1575.670457	208.4600412	3.957269149	NSGA-II	
11.40552918	3.416383407	0.378148558	1575.431162	207.515325	4.503704925	GWO	
11.42098671	3.426018563	0.378103784	1575.280324	207.50153	4.5115565	GWO	
11.41561098	3.438929504	0.37812805	1575.263498	207.5049884	4.508783817	GWO	
10.3013012	3.449641117	0.379705151	1574.701562	208.42438	3.976271602	GWO	

SOI (°BTDC)	PRc	m_f (g/Cycle)	$\bar{P}_{eng}$ (kW)	BSFC (g/kWh)	NO_x (g/kWh)	Algorithm	Selected Point
12.25312926	3.410352313	0.376800432	1574.6596	206.8784417	4.937365093	GWO	
10.39031572	3.462123984	0.379546252	1574.553617	208.3480661	4.016710252	NSGA-II	
12.07306051	3.423232399	0.376972413	1574.28823	207.0120646	4.844728053	GWO	
15.70097731	3.114124208	0.372980646	1574.011238	204.7060206	6.7562114	GWO	
9.804382025	3.402493147	0.380335448	1573.965276	208.9036001	3.75987472	NSGA-II	
9.680841096	3.371876066	0.380431089	1573.378215	209.0688842	3.708556596	GA	
9.925044666	3.432874798	0.379981593	1573.315193	208.7688204	3.811906477	NSGA-II	
10.49996993	3.438444227	0.379002102	1573.114735	208.2690796	4.068636007	NSGA-II	
9.843857886	3.432921876	0.379954296	1572.620544	208.844997	3.777847114	NSGA-II	
9.705760489	3.400322951	0.38012825	1572.372318	209.0044786	3.719928631	GA	
10.07557336	3.500036882	0.379526296	1571.991058	208.6465828	3.878114816	NSGA-II	
15.39832714	3.100863085	0.372668232	1571.309002	204.8778981	6.5919609	GWO	
10.02219922	3.506561876	0.379392394	1570.98107	208.704847	3.855685821	NSGA-II	
10.73822854	3.468699455	0.378141701	1570.79601	208.0872183	4.182356313	GWO	
10.0776024	3.44950139	0.379147517	1570.784827	208.6443493	3.880549311	NSGA-II	
9.963531556	3.44950139	0.379147517	1569.985848	208.7491742	3.831604403	NSGA-II	
9.1706329	3.329041493	0.380439422	1569.248513	209.6642488	3.507785725	GWO	
9.192461222	3.411496697	0.380252582	1569.093072	209.4762026	3.516702638	NSGA-II	
9.587130927	3.274996774	0.379770965	1569.034452	209.4226713	3.673010542	NSGA-II	
9.549425147	3.467109822	0.379547595	1568.63797	209.1190077	3.658676453	NSGA-II	
15.52131974	3.129033201	0.371847935	1568.589875	204.8126042	6.664683977	GWO	
9.339640388	3.457093092	0.379756058	1568.036549	209.3118967	3.574999231	NSGA-II	
9.333644658	3.46496027	0.379772594	1568.026965	209.3151593	3.572609486	NSGA-II	
9.156287861	3.292743977	0.380180853	1567.650161	209.7898567	3.503273128	GWO	
9.127733719	3.464845001	0.379954296	1567.266694	209.5048518	3.49331808	NSGA-II	
15.46086715	3.101992833	0.371430079	1566.250871	204.8376662	6.634264272	GWO	
9.104328322	3.345711838	0.379760456	1566.044108	209.6972939	3.485218781	GWO	
8.902867931	3.43397708	0.379981013	1565.751905	209.7372108	3.410429151	NSGA-II	
15.23321818	3.10953946	0.371483836	1565.647683	204.9743889	6.509970215	GWO	
16.89350598	3.067235645	0.370191823	1565.437462	204.0986257	7.462036148	NSGA-II	
15.14375465	3.123955633	0.371480825	1565.428876	205.0297462	6.461738515	GWO	
17.34143276	3.066166115	0.36974676	1564.72713	203.9253535	7.72998802	NSGA-II	
9.458671243	3.511095042	0.378838656	1564.597377	209.2476472	3.625124291	NSGA-II	
8.963072032	3.475923514	0.379541521	1564.224417	209.6742836	3.433752073	NSGA-II	
16.43486599	3.063933969	0.370172865	1563.869859	204.3067349	7.193903353	NSGA-II	
15.22317927	3.102784194	0.370931539	1563.137208	204.9807364	6.508043914	GWO	
16.21461119	3.058127983	0.370172865	1563.025262	204.4203818	7.066633424	NSGA-II	
8.761367049	3.428475689	0.379573778	1562.943817	209.8907549	3.361336518	NSGA-II	
9.065918303	3.437245107	0.378958136	1562.662271	209.6069295	3.473663642	NSGA-II	
8.623990429	3.388731273	0.379756147	1562.542804	210.0763086	3.313094555	NSGA-II	

SOI (°BTDC)	PRc	m_f (g/Cycle)	$\bar{P}_{eng}$ (kW)	BSFC (g/kWh)	NO_x (g/kWh)	Algorithm	Selected Point
8.617994699	3.312981579	0.379772683	1561.937191	210.2685335	3.310992923	NSGA-II	
8.463472104	3.485105051	0.379755854	1561.24777	210.1482084	3.259080482	GA	
8.519923658	3.459158638	0.379610035	1561.178764	210.1021391	3.278310712	NSGA-II	
8.777842638	3.485207454	0.378935374	1560.187275	209.8739718	3.369208801	NSGA-II	
8.44045697	3.504060526	0.379392394	1559.400912	210.1901245	3.252568942	NSGA-II	
16.90709213	3.0679569	0.368612018	1558.607492	204.097171	7.483728953	NSGA-II	
8.221758919	3.475388978	0.379510425	1558.354599	210.391046	3.181951801	NSGA-II	
16.21461119	3.058127983	0.368929475	1557.638165	204.419131	7.076084433	NSGA-II	
7.997277481	3.262695982	0.379987944	1557.000108	211.063557	3.112318993	NSGA-II	
8.125882094	3.501290666	0.379395289	1556.963915	210.4934329	3.152594177	NSGA-II	
8.042014219	3.434861322	0.379395289	1556.496543	210.5916258	3.127208715	NSGA-II	
8.324644566	3.534481293	0.378838656	1555.851104	210.3518498	3.216518937	NSGA-II	
8.362616384	3.423704269	0.378601129	1555.698649	210.3116715	3.229473682	GWO	
7.907504247	3.484667295	0.379350523	1555.123489	210.7030717	3.087762182	NSGA-II	
8.195318064	3.501503983	0.378789878	1554.938519	210.4489527	3.175724146	NSGA-II	
8.644677946	3.484820731	0.377810161	1554.364471	210.0425075	3.32632735	GWO	
7.761282454	3.516222299	0.379387584	1553.899261	210.8581735	3.046301072	NSGA-II	
7.611684516	3.484667295	0.379394057	1552.900882	210.9908059	3.005781226	NSGA-II	
7.514423713	3.378552514	0.379584455	1552.70935	211.1952607	2.980008377	GA	
7.750377429	3.404411893	0.378986174	1552.314629	210.9285171	3.044288775	NSGA-II	
7.391114801	3.504060526	0.379525796	1551.541329	211.2070564	2.949202782	NSGA-II	
7.564554857	3.400812706	0.378933845	1550.535275	211.1190838	2.994501983	NSGA-II	
7.513879729	3.404411893	0.37891954	1550.068364	211.1636392	2.981426321	NSGA-II	
7.17436263	3.306677558	0.37937918	1548.170881	211.737318	2.89831883	NSGA-II	
7.017388715	3.432477336	0.379320363	1547.654593	211.6033366	2.863934163	GA	
7.003417236	3.494704329	0.379353851	1547.618464	211.589979	2.860900786	GA	
7.279602693	3.504060526	0.378789878	1547.499301	211.345075	2.92397038	NSGA-II	
7.088584106	3.436536565	0.378921202	1546.590509	211.541479	2.880149265	NSGA-II	
6.919158876	3.4611417	0.378902175	1545.080893	211.6915385	2.844292171	NSGA-II	
6.759570885	3.433009683	0.379148312	1544.718385	211.8610418	2.812366517	GA	
6.531322969	3.464882339	0.37880491	1541.328764	212.0734251	2.772027701	NSGA-II	
6.662669699	3.409898877	0.378485033	1541.004274	212.0052242	2.795643868	NSGA-II	
6.442043389	3.459259753	0.37888238	1540.879091	212.160207	2.757138577	GA	
6.497728616	3.472104912	0.378757903	1540.831438	212.1061527	2.766476134	GA	
6.459175569	3.447775849	0.378685861	1540.19323	212.1568642	2.760261334	GA	
6.391986396	3.331361315	0.378816788	1539.311429	212.4404931	2.749298452	NSGA-II	
6.372490447	3.242939694	0.378755361	1537.418981	212.7817627	2.746367485	NSGA-II	
6.402127966	3.408890816	0.377981305	1536.603432	212.2763158	2.752359797	NSGA-II	
6.375141569	3.272264036	0.37819056	1535.664538	212.6689087	2.747762424	NSGA-II	
6.35173547	3.163451251	0.378641255	1534.907194	213.1667014	2.743367891	NSGA-II	
6.342690221	3.121417516	0.378660436	1533.719296	213.3899209	2.741953527	NSGA-II	

SOI (°BTDC)	PRc	m_f (g/Cycle)	$\bar{P}_{eng}$ (kW)	BSFC (g/kWh)	NO_x (g/kWh)	Algorithm	Selected Point
6.342241926	3.120802899	0.378660436	1533.696854	213.3936097	2.741885263	NSGA-II	
6.33882015	3.086494302	0.378409225	1531.574004	213.5832693	2.741797653	NSGA-II	
6.324924979	3.047816466	0.378498662	1530.481471	213.8187938	2.739539662	NSGA-II	
6.320041347	3.062652956	0.377774641	1528.035057	213.7372148	2.740053932	NSGA-II	
6.310812339	3.002214795	0.378304059	1527.835523	214.1118606	2.737754406	NSGA-II	
6.310812339	3.002647464	0.378276469	1527.742203	214.1090837	2.737801781	NSGA-II	
6.305761442	2.96370587	0.378275022	1526.057446	214.3681051	2.737049772	NSGA-II	
6.302193063	2.946429454	0.378331011	1525.475057	214.4892511	2.736422237	NSGA-II	
6.293729961	2.913238584	0.378523277	1524.586304	214.7320599	2.734838295	NSGA-II	
6.293729961	2.913238584	0.37852176	1524.580297	214.7320563	2.734840878	NSGA-II	
6.288796526	2.87900823	0.378367193	1522.173446	214.9889897	2.734375208	NSGA-II	
6.286662211	2.856999424	0.378412051	1521.133843	215.1594321	2.733984033	NSGA-II	
6.283633657	2.850429409	0.378423708	1520.783351	215.2135976	2.733518324	NSGA-II	
6.273242672	2.825970466	0.378464395	1519.428231	215.4179747	2.731925851	NSGA-II	
6.273258865	2.869978001	0.377429299	1517.849484	215.0703782	2.733697739	NSGA-II	
6.273258865	2.86906632	0.377429299	1517.800636	215.0773225	2.733697738	NSGA-II	
6.261575465	2.775293419	0.378426594	1515.986697	215.849864	2.730290895	NSGA-II	
6.26279095	2.77663154	0.378078426	1514.738627	215.8357446	2.731057805	NSGA-II	
6.249494492	2.737261979	0.378168548	1512.259849	216.1939588	2.728980238	NSGA-II	
6.249494492	2.733612893	0.378168548	1511.997483	216.2268236	2.728980235	NSGA-II	
6.249711819	2.737261979	0.377956103	1511.445961	216.1925579	2.729371739	NSGA-II	
6.243304922	2.702470424	0.378275973	1510.027643	216.5213387	2.727908512	NSGA-II	
6.243304922	2.707122541	0.377895792	1508.935514	216.4748287	2.728551694	NSGA-II	
6.243350217	2.682633791	0.378337859	1508.700562	216.7124606	2.727810689	NSGA-II	
6.243350217	2.678539754	0.378337859	1508.369919	216.7526104	2.727810686	NSGA-II	
6.243350217	2.666826007	0.378337859	1507.408273	216.8690796	2.727810676	NSGA-II	
6.243350217	2.660353979	0.378337859	1506.86688	216.9344886	2.727810671	NSGA-II	
6.235760674	2.65330436	0.378338784	1506.203345	217.0141543	2.726722598	NSGA-II	
6.235760674	2.6419754	0.378338784	1505.223975	217.1321633	2.726722589	NSGA-II	
6.234214373	2.635893264	0.378306123	1504.552746	217.197752	2.726556751	NSGA-II	
6.228075469	2.616033855	0.378213948	1502.360776	217.4186975	2.725837282	NSGA-II	
6.228075469	2.616033855	0.378073203	1501.838499	217.4166933	2.726074179	NSGA-II	
6.21826975	2.600456919	0.378175669	1500.672897	217.6039122	2.724511564	NSGA-II	
6.21826975	2.60033519	0.378175669	1500.661329	217.6053128	2.724511564	NSGA-II	
6.214681729	2.584550016	0.378141654	1498.979282	217.7933268	2.724062092	NSGA-II	
6.214681729	2.584550016	0.378138195	1498.966585	217.7932649	2.724067893	NSGA-II	
6.214272164	2.571359345	0.378165063	1497.749601	217.9543273	2.723965085	NSGA-II	
6.213041636	2.561756739	0.378173461	1496.791665	218.075732	2.723777609	NSGA-II	
6.213041636	2.554919927	0.378180986	1496.111433	218.1631858	2.723764996	NSGA-II	
6.206711204	2.54926571	0.378053365	1494.998928	218.239965	2.723088803	NSGA-II	

SOI (°BTDC)	PRc	m_f (g/Cycle)	$\bar{P}_{eng}$ (kW)	BSFC (g/kWh)	NO_x (g/kWh)	Algorithm	Selected Point
6.206238611	2.531022967	0.378078562	1493.130009	218.4853028	2.722980258	NSGA-II	
6.200316871	2.513422168	0.378078426	1491.119823	218.7388674	2.722151299	NSGA-II	
6.200316871	2.508202095	0.378078426	1490.526472	218.8147176	2.722151295	NSGA-II	
6.19554397	2.502853796	0.378058	1489.796146	218.8977493	2.72151939	NSGA-II	
6.194527644	2.49308023	0.37818225	1489.087534	219.0500699	2.721170496	NSGA-II	
6.195579012	2.502325015	0.37774038	1488.605658	218.8958465	2.722056389	NSGA-II	
6.191319421	2.478278707	0.37815024	1487.175629	219.2836192	2.720777713	NSGA-II	
6.192537186	2.478278707	0.378121952	1487.087244	219.2814095	2.720994111	NSGA-II	
6.18811327	2.464289963	0.378187488	1485.556841	219.5161666	2.720270781	NSGA-II	
6.18811327	2.45913139	0.378187488	1484.910554	219.6025948	2.720270777	NSGA-II	
6.186881676	2.4480568	0.378178515	1483.459011	219.7933429	2.720115046	NSGA-II	

Appendix D

Appendix D.1. Alternatives, Criteria, ERM and PDM for SIMUS

Alt	SOI (°BTDC)	PRc	m_f (g/Cycle)	Peng (kW)	BSFC (g/kW)	NO_x (g/kWh)	ERM Score	ERM Rank	Net Dominance	PDM Rank
A4 (K)	12.706	3.430	0.380	1588.61	206.48	5.156	1.309	1	11.40	1
A6	10.564	3.499	0.380	1576.53	208.20	4.094	0.922	2	7.14	2
A7	9.192	3.411	0.379	1569.09	209.48	3.517	0.769	3	5.46	3
A3	13.998	3.374	0.379	1593.87	205.68	5.819	0.000	4	−3.00	4
A2	15.388	3.183	0.379	1598.99	204.92	6.545	0.000	4	−3.00	4
A1	18.415	3.055	0.379	1606.36	203.61	8.249	0.000	4	−3.00	4
A5	17.711	3.046	0.374	1583.04	203.78	7.906	0.000	4	−3.00	4
A8	8.222	3.475	0.380	1558.36	210.39	3.182	0.000	4	−3.00	4
A9	6.459	3.448	0.379	1540.19	212.16	2.760	0.000	4	−3.00	4
A10	6.243	2.702	0.378	1510.03	216.52	2.728	0.000	4	−3.00	4
A11	6.187	2.448	0.378	1483.46	219.79	2.720	0.000	4	−3.00	4

Appendix D.2. TOPSIS Rankings

Vector-Normalized Rank	Alternative	Vector-Normalized C_i*	Min–Max Rank	Min–Max Normalized C_i*
1	A9	0.9470	7	0.6124
2	A10	0.9244	10	0.4822
3	A8	0.9077	5	0.6825
4	A11	0.9063	11	0.4142
5	A7	0.8528	3	0.7205
6	A6	0.7513	1	0.7413
7	**A4 (K)**	**0.5622**	**2**	**0.7255**
8	A3	0.4447	4	0.6945
9	A2	0.3182	6	0.6589
10	A5	0.1067	9	0.5723
11	A1	0.0937	8	0.5858

Appendix D.3. Sensitivity Analysis

% Perturbation	First	Second	Third	Fourth	Fifth-Eleventh
−15%	A6	A7	A4 (K)	A3	A2, A1, A5, A8, A9, A10, A11
−10%	A6	A7	A4 (K)	A3	A2, A1, A5, A8, A9, A10, A11
−5%	A6	A4 (K)	A7	A3	A2, A1, A5, A8, A9, A10, A11
0%	A4 (K)	A6	A7	A3	A2, A1, A5, A8, A9, A10, A11
+5%	A4 (K)	A7	A6	A3	A2, A1, A5, A8, A9, A10, A11
+10%	A4 (K)	A7	A3	A6	A2, A1, A5, A8, A9, A10, A11
+15%	A3	A4 (K)	A7	A6	A2, A1, A5, A8, A9, A10, A11

References

1. Natural Resources Canada. Northern, Indigenous, Rural, and Remote Communities. 2025. Available online: https://natural-resources.canada.ca/science-data/science-research/research-centres/northern-indigenous-rural-remote-communities (accessed on 6 October 2026).
2. Pinto, H.; Gates, I.D. Why is it so difficult to replace diesel in Nunavut, Canada? *Renew. Sustain. Energy Rev.* **2022**, *157*, 112030. [CrossRef]
3. Kalantari, H.; Ghoreishi-Madiseh, S.A. Hybrid Renewable Hydrogen Energy Solution for Remote Cold-Climate Open-Pit Mines. *Hydrogen* **2022**, *3*, 312–332. [CrossRef]
4. Gharali, K.; Sarshar, S.; Rafiei, B.; Bahreinian, S.; Fraser, R.; Dusseault, M.B.; Nathwani, J.; Soltani, M. Renewable energy impacts on Canada's remote areas: A review study. *Energy Strategy Rev.* **2026**, *63*, 102006. [CrossRef]
5. Huang, H. Decarbonising Australia's Critical Minerals Mining via Hybrid Microgrid. Ph.D. Thesis, The University of New South Wales, Sydney, Australia, 2025. [CrossRef]
6. Basbous, T.; Younes, R.; Ilinca, A.; Perron, J. Optimal management of compressed air energy storage in a hybrid wind-pneumatic-diesel system for remote area's power generation. *Energy* **2015**, *84*, 267–278. [CrossRef]
7. Fang, Y.; Lu, Y.; Yu, X.; Su, L.; Fan, Z.; Huang, R.; Roskilly, A.P. Study of a hybrid pneumatic-combustion engine under steady-state and transient conditions for transport application. *Int. J. Engine Res.* **2019**, *22*, 528–539. [CrossRef]
8. Mollenhauer, K.; Tschöke, H. (Eds.) *Handbook of Diesel Engines*; Springer: Berlin/Heidelberg, Germany, 2010.
9. Guan, W.; Pedrozo, V.; Zhao, H.; Ban, Z.; Lin, T. *Exploring the NOx Reduction Potential of Miller Cycle and EGR on a HD Diesel Engine Operating at Full Load*; SAE Technical Paper Series; SAE International: Warrendale, PA, USA, 2018.
10. Hong, L.J.; Zhang, X. Surrogate-Based Simulation Optimization. In *Tutorials in Operations Research: Emerging Optimization Methods and Modeling Techniques with Applications*; Institute for Operations Research and the Management Sciences (INFORMS): Catonsville, MD, USA, 2021; pp. 287–311.
11. Pal, A.; Zhu, L.; Wang, Y.; Zhu, G. Constrained Surrogate-Based Engine Calibration Using Lower Confidence Bound. *IEEE/ASME Trans. Mechatron.* **2021**, *26*, 3116–3127. [CrossRef]
12. Holdmann, G.; Pride, D.; Poelzer, G.; Noble, B.; Walker, C. Critical pathways to renewable energy transitions in remote Alaska communities: A comparative analysis. *Energy Res. Soc. Sci.* **2022**, *91*, 102712. [CrossRef]
13. Hosseini, M.; Lubitz, W.D.; Tasnim, S.H.; Mahmud, S. Optimization of hybrid renewable energy systems for remote communities in northern Canada. *Renew. Energy* **2025**, *244*, 122729. [CrossRef]
14. Quitoras, M.R.; Campana, P.E.; Crawford, C. Exploring electricity generation alternatives for Canadian Arctic communities using a multi-objective genetic algorithm approach. *Energy Convers. Manag.* **2020**, *210*, 112471. [CrossRef]
15. Yaïci, W.; Longo, M. Microgrid hybrid renewable energy systems with hydrogen and battery storage options for residential buildings: A feasibility analysis in Canada. *J. Clean. Prod.* **2025**, *519*, 145974. [CrossRef]
16. Isherwood, W.; Smith, J.R.; Aceves, S.M.; Berry, G.; Clark, W.; Johnson, R.; Das, D.; Goering, D.; Seifert, R. Remote power systems with advanced storage technologies for Alaskan villages. *Energy* **2000**, *25*, 1005–1020. [CrossRef]
17. Khalaf, S. Integration of Distributed Diesel Generators in Power System, Iraq Case Study. Ph.D. Thesis, Cardiff University, Cardiff, UK, 2021. Available online: https://orca.cardiff.ac.uk/id/eprint/149179 (accessed on 6 October 2026).
18. Ngwaka, U.; Chen, F.; Qiu, S.; Li, M.; Zhang, C.; Wu, D. Recent progress on performance and control of linear engine generator. *Int. J. Engine Res.* **2022**, *24*, 2866–2896. [CrossRef]
19. Purbandono, D.A.; Budiyanto, M.A.; Ramdan, F.; Felani, M.I. Optimization of load distribution and fuel consumption for diesel generator 1000 kW for remote area using biodiesel B35 power station. *East.-Eur. J. Enterp. Technol.* **2025**, *3*, 42–59. [CrossRef]
20. Richard, W.; Ron, J. *Effects of Village Power Quality on Fuel Consumption and Operating Expenses*; OSTI.GOV, Ed.; University of Alaska: Fairbanks, AK, USA, 2008.

21. Queipo, N.V.; Haftka, R.T.; Shyy, W.; Goel, T.; Vaidyanathan, R.; Kevin Tucker, P. Surrogate-based analysis and optimization. *Prog. Aerosp. Sci.* **2005**, *41*, 1–28. [CrossRef]
22. Bauman Moscow State Technical University. *Diesel-RK*; Bauman Moscow State Technical University: Moscow, Russia, 2023.
23. Juma, A.L.H.; Parida, M.K.; Joardar, H. Numerical Investigation of Combustion Characteristics for Soybean Biodiesel Depending on Variable Compression Ratios by Using Diesel RK Software. In *Evolutionary Manufacturing, Design and Operational Practices for Resource and Environmental Sustainability*; Wiley: Hoboken, NJ, USA, 2024; pp. 163–176.
24. Pal, M.K.; Reddy, E.R. Application of Diesel-RK Simulation Tool for Reducing NOx Emission from Biodiesel Blend Fuels at Retarded Injection Condition. *Int. J. Energy A Clean Environ.* **2024**, *25*, 83–95. [CrossRef]
25. Shah, S.; Patel, N. Optimizing Diesel Engine Combustion Performance and Emissions with Diesel-RK Software Simulation. *J. Mines Met. Fuels* **2025**, 2221–2231. [CrossRef]
26. Mukherjee, K.; Bhattacharjee, P.; Ghosh, S.; Dhara, S.; Bhadra, S.; Das, M.C. Exploration of Diesel—RK simulation tool to determine the emission characteristics for various blends of jatropha biodiesel with lemon peel oil and conventional diesel. In Proceedings of the 2025 International Conference on Sustainable Technology in Energy and Power Systems (STEPCon), Kolkata, India, 20–21 November 2025; pp. 29–34.
27. Polat, F. Investigation of the effect of compression ratio on the emission and performance characteristics of diesel engines with using Diesel RK software. *Gümüşhane Üniversitesi Fen Bilim. Derg.* **2022**, *12*, 826–838. [CrossRef]
28. Musthafa, B.; Saravanan, B.; Vaibhav, B.; Muhammad, P.; Sam, F.; Asokan, M.A. Performance and emission analysis of a diesel engine fuelled with Juliflora biodiesel: A simulation and experimental study. *Aust. J. Mech. Eng.* **2023**, *23*, 220–234. [CrossRef]
29. Li, Y.; Sciacovelli, A.; Peng, X.; Radcliffe, J.; Ding, Y. Integrating compressed air energy storage with a diesel engine for electricity generation in isolated areas. *Appl. Energy* **2016**, *171*, 26–36. [CrossRef]
30. Wang, L.; Li, D.-F.; Xu, H.-X.; Fan, Z.-P.; Dou, W.-B.; Yu, X.-L. Research on a pneumatic hybrid engine with regenerative braking and compressed-air-assisted cranking. *Proc. Inst. Mech. Eng. Part D* **2015**, *230*, 406–422. [CrossRef]
31. Basbous, T. Hybridation Pneumatique d'un Moteur Diesel en vue de son Utilisation dans un Système Hybride Éolien-Diesel avec Stockage d'Énergie sous Forme d'Air Comprimé. Ph.D. Thesis, Université du Québec à Chicoutimi, Chicoutimi, QC, Canada, 2013. Available online: https://constellation.uqac.ca/id/eprint/2673/ (accessed on 6 October 2026).
32. Basbous, T.; Younes, R.; Ilinca, A.; Perron, J. A new hybrid pneumatic combustion engine to improve fuel consumption of wind–Diesel power system for non-interconnected areas. *Appl. Energy* **2012**, *96*, 459–476. [CrossRef]
33. Basbous, T.; Younes, R.; Ilinca, A.; Perron, J. Pneumatic hybridization of a diesel engine using compressed air storage for wind-diesel energy generation. *Energy* **2012**, *38*, 264–275. [CrossRef]
34. Ibrahim, H. Étude et Conception d'un Générateur Hybride d'Électricité de Type Éolien-Diesel avec Élément de Stockage d'Air Comprimé. Ph.D. Thesis, Université du Québec à Chicoutimi, Chicoutimi, QC, Canada, 2010. Available online: https://constellation.uqac.ca/281/ (accessed on 6 October 2026).
35. Ibrahim, H.; Issa, M.; Lepage, R.; Ilinca, A.; Perron, J. Supercharging of Diesel Engine with Compressed Air: Experimental Investigation on Greenhouse Gases and Performance for a Hybrid Wind-Diesel System. *Smart Grid Renew. Energy* **2019**, *10*, 213–236. [CrossRef]
36. Saad, Y.; Younes, R.; Abboudi, S.; Ilinca, A. Hydro-pneumatic storage for wind-diesel electricity generation in remote sites. *Appl. Energy* **2018**, *231*, 1159–1178. [CrossRef]
37. Martinez, N.; Benchaabane, Y.; Silva, R.E.; Ilinca, A.; Ibrahim, H.; Chandra, A.; Rousse, D.R. Computer Model for a Wind–Diesel Hybrid System with Compressed Air Energy Storage. *Energies* **2019**, *12*, 3542. [CrossRef]
38. Kim, N.H. *Surrogate Modeling and Optimization*; Wiley: Hoboken, NJ, USA, 2025.
39. Garud, S.S.; Karimi, I.A.; Kraft, M. Design of computer experiments: A review. *Comput. Chem. Eng.* **2017**, *106*, 71–95. [CrossRef]
40. Liang, J.; Li, Z.; Pan, L.; Khailah, E.Y.; Sun, L.; Lu, W. Research on surrogate model of dam numerical simulation with multiple outputs based on adaptive sampling. *Sci. Rep.* **2023**, *13*, 11955. [CrossRef] [PubMed]
41. Sun, X.; Croke, B.; Roberts, S.; Jakeman, A. Investigation of determinism-related issues in the Sobol′ low-discrepancy sequence for producing sound global sensitivity analysis indices. *ANZIAM J.* **2021**, *62*, C84–C97. [CrossRef]
42. Navid, A.; Khalilarya, S.; Abbasi, M. Diesel engine optimization with multi-objective performance characteristics by non-evolutionary Nelder-Mead algorithm: Sobol sequence and Latin hypercube sampling methods comparison in DoE process. *Fuel* **2018**, *228*, 349–367. Correction in *Fuel* **2019**, *243*, 659. [CrossRef]
43. Chan, Y.K.; Poon, H.M.; Jauw, V.L. Development of intelligent learning-based surrogate models for predicting diesel ignition at different thermodynamic conditions. *Energy Convers. Manag.* **2026**, *348*, 120638. [CrossRef]
44. Ma, Y.; Zhao, Y.; Yang, D.; E, J.; Zhao, J.; Pan, M. Parametric study of combustion characteristics of diesel/methanol dual fuel engine using global sensitivity analysis and multi-objective optimization. *Renew. Energy* **2024**, *237*, 121690. [CrossRef]
45. Li, J.; Zhang, Z.; Ye, Y.; Li, W.; Yuan, T.; Wang, H.; Li, Y.; Tan, D.; Zhang, C. Effects of different injection timing on the performance, combustion and emission characteristics of diesel/ethanol/n-butanol blended diesel engine based on multi-objective optimization theory. *Energy* **2022**, *260*, 125056. [CrossRef]

46. Jafaryeganeh, H.; Ventura, M.; Guedes Soares, C. Effect of normalization techniques in multi-criteria decision making methods for the design of ship internal layout from a Pareto optimal set. *Struct. Multidiscip. Optim.* **2020**, *62*, 1849–1863. [CrossRef]
47. Rao, R.V.; Lakshmi, R.J. Ranking of Pareto-optimal solutions and selecting the best solution in multi- and many-objective optimization problems using R-method. *Soft Comput. Lett.* **2021**, *3*, 100015. [CrossRef]
48. Munier, N. Strategic Approach in Multi-Criteria Decision Making. In *International Series in Operations Research & Management Science*; Springer: Berlin/Heidelberg, Germany, 2024.
49. Basakayi, J.K.; Tshitshonu, E.K.; Rousse, D.R.; Ilinca, A. Dynamic multicriteria ranking of energy storage systems using a linear programming-based decision framework. *J. Energy Storage* **2026**, *161*, 121892. [CrossRef]
50. Basakayi, J.K.; Tshitshonu, E.K.; Ilinca, A. Bayesian Optimization-Based Performance Enhancement of Pneumatic-Hybrid Diesel Generators for Remote Power Systems. In Proceedings of the 3rd International Online Conference on Energies, Virtual Event, 12–15 May 2026.
51. *SAE J1995_202509*; Engine Power Test Code—Spark Ignition and Compression Ignition—Gross Power and Torque Rating. SAE International: Warrendale, PA, USA, 2025. [CrossRef]
52. Antony, J. *Design of Experiments for Engineers and Scientists*; Butterworth-Heinemann: Oxford, UK; Burlington, MA, USA, 2003.
53. Rasmussen, C.E.; Williams, C.K.I. Gaussian Processes for Machine Learning. In *Adaptive Computation and Machine Learning*; MIT Press: Cambridge, MA, USA, 2006.
54. Herman, J.; Usher, W. SALib: An open-source Python library for Sensitivity Analysis. *J. Open Source Softw.* **2017**, *2*, 97. [CrossRef]
55. Wolpert, D.H.; Macready, W.G. No free lunch theorems for optimization. *IEEE Trans. Evol. Comput.* **1997**, *1*, 67–82. [CrossRef]
56. Ahmed, F.; Deb, K. Multi-objective optimal path planning using elitist non-dominated sorting genetic algorithms. *Soft Comput.* **2012**, *17*, 1283–1299. [CrossRef]
57. Bamshad, A. Toward sustainable power generation: Techno-Economic optimization of a solar-driven ORC power plant with integrated desalination and hydrogen backup. *Unconv. Resour.* **2026**, *12*, 100366. [CrossRef]
58. Bian, C.; Qian, C. Better Running Time of the Non-dominated Sorting Genetic Algorithm II (NSGA-II) by Using Stochastic Tournament Selection. In *Parallel Problem Solving from Nature—PPSN XVII*; ACM: New York, NY, USA, 2022; pp. 428–441.
59. Zhang, Y. Multi-objective diesel engine emission management and control technology based on SVM and NSGA-II. *Results Eng.* **2023**, *20*, 101581. [CrossRef]
60. Blank, J.; Deb, K. Pymoo: Multi-Objective Optimization in Python. *IEEE Access* **2020**, *8*, 89497–89509. [CrossRef]
61. Chen, G.; Hu, D.; Chien, S. Optimizing Battery-Electric-Feeder Service and Wireless Charging Locations with Nested Genetic Algorithm. *IEEE Access* **2020**, *8*, 67166–67178. [CrossRef]
62. Eweis-Labolle, J.T.; Zhao, C.; Won, Y.; Bostanabad, R. Multi-Fidelity Design of Porous Microstructures for Thermofluidic Applications. *J. Mech. Des.* **2024**, *146*, 1–29. [CrossRef]
63. Rodríguez del Nozal, A.; Tapia, A.; Alvarado-Barrios, L.; Reina, D.G. Application of Genetic Algorithms for Unit Commitment and Economic Dispatch Problems in Microgrids. In *Nature Inspired Computing for Data Science*; Springer: Berlin/Heidelberg, Germany, 2020; pp. 139–167.
64. Mirjalili, S.; Mirjalili, S.M.; Lewis, A. Grey Wolf Optimizer. *Adv. Eng. Softw.* **2014**, *69*, 46–61. [CrossRef]
65. Mirjalili, S.; Saremi, S.; Mirjalili, S.M.; Coelho, L.d.S. Multi-objective grey wolf optimizer: A novel algorithm for multi-criterion optimization. *Expert Syst. Appl.* **2016**, *47*, 106–119. [CrossRef]
66. Wei, F.; Zhang, Z.; Wei, W.; Zhang, H.; Cai, W.; Dong, D.; Li, G. Multi-objective optimization of the performance for a marine methanol-diesel dual-fuel engine. *Fuel* **2024**, *368*, 131556. [CrossRef]
67. Zhu, W.; Guo, J.; Zhao, G.; Zeng, B. Optimal Sizing of an Island Hybrid Microgrid Based on Improved Multi-Objective Grey Wolf Optimizer. *Processes* **2020**, *8*, 1581. [CrossRef]
68. Lv, L.; Yang, L.; Pan, J.-S.; Liu, D.; Cui, Z.; Wang, H.; Xie, H. Constrained multi-objective wolf pack algorithm based on cooperative optimization and tiered hunting. *J. King Saud Univ. Comput. Inf. Sci.* **2026**, *38*, 219. [CrossRef]
69. Palm, N.; Landerer, M.; Palm, H. Gaussian Process Regression Based Multi-Objective Bayesian Optimization for Power System Design. *Sustainability* **2022**, *14*, 12777. [CrossRef]
70. Yu, J.; Chen, R.; Li, Y.; Kang, M.; Yu, S. A Multi-objective Optimization Algorithm for Air-path System of Diesel Engines. *IFAC-Pap.* **2021**, *54*, 90–95. [CrossRef]
71. Zhou, Q.; Zhao, M.; Hu, J.; Ma, M. *Multi-fidelity Surrogates*; Engineering Applications of Computational Methods; Springer: Singapore, 2023.

Disclaimer/Publisher's Note: The statements, opinions and data contained in all publications are solely those of the individual author(s) and contributor(s) and not of MDPI and/or the editor(s). MDPI and/or the editor(s) disclaim responsibility for any injury to people or property resulting from any ideas, methods, instructions or products referred to in the content.